



Structural determinants of a conserved enantiomer-selective carvone binding pocket in the human odorant receptor OR1A1

Christiane Geithe¹ · Jonas Protze² · Franziska Kreuchwig^{2,3} ·
Gerd Krause² · Dietmar Krautwurst¹

Received: 21 March 2017 / Revised: 29 May 2017 / Accepted: 16 June 2017 / Published online: 27 June 2017
© Springer International Publishing AG 2017

Abstract Chirality is a common phenomenon within odorants. Most pairs of enantiomers show only moderate differences in odor quality. One example for enantiomers that are easily discriminated by their odor quality is the carvones: humans significantly distinguish between the spearmint-like (*R*)-(−)-carvone and caraway-like (*S*)-(+)-carvone enantiomers. Moreover, for the (*R*)-(−)-carvone, an anosmia is observed in about 8% of the population, suggesting enantioselective odorant receptors (ORs). With only about 15% de-orphaned human ORs, the lack of OR crystal structures, and few comprehensive studies combining in silico and experimental approaches to elucidate structure–function relations of ORs, knowledge on cognate odorant/OR interactions is still sparse. An adjusted homology modeling approach considering OR-specific proline-caused conformations, odorant docking studies, single-nucleotide polymorphism (SNP) analysis, site-directed mutagenesis, and subsequent functional studies with recombinant ORs in a cell-based, real-time luminescence assay revealed 11 amino acid positions to constitute an

enantioselective binding pocket necessary for a carvone function in human OR1A1 and murine Olfr43, respectively. Here, we identified enantioselective molecular determinants in both ORs that discriminate between minty and caraway odor. Comparison with orthologs from 36 mammalian species demonstrated a hominid-specific carvone binding pocket with about 100% conservation. Moreover, we identified loss-of-function SNPs associated with the carvone binding pocket of OR1A1. Given carvone enantiomer-specific receptor activation patterns including OR1A1, our data suggest OR1A1 as a candidate receptor for constituting a carvone enantioselective phenotype, which may help to explain mechanisms underlying a (*R*)-(−)-carvone-specific anosmia in humans.

Keywords Structure–function study · Molecular modeling · Site-directed mutagenesis · GPCR · Ortholog

Abbreviations

AA	Amino acid
ECL	Extracellular loop
GPCR	G-protein coupled receptor
KFO	Key food odorant
OR	Odorant receptor
SNP	Single-nucleotide polymorphism
TMH	Transmembrane helix

Electronic supplementary material The online version of this article (doi:[10.1007/s00018-017-2576-z](https://doi.org/10.1007/s00018-017-2576-z)) contains supplementary material, which is available to authorized users.

✉ Gerd Krause
GKrause@fmp-berlin.de

Dietmar Krautwurst
dietmar.krautwurst@lrz.tum.de

¹ Deutsche Forschungsanstalt für Lebensmittelchemie Leibniz Institut (DFA), Freising, Germany

² Leibniz-Forschungsinstitut für Molekulare Pharmakologie (FMP), Berlin, Germany

³ Present Address: Max-Delbrück-Centrum für Molekulare Medizin (MDC), Berlin, Germany

Introduction

The chemical sense of smell enables detection and discrimination of thousands of structurally diverse odorants, especially of about 230 so far identified aroma-determining

key food odorants (KFOs) [1, 2], which are the basis for developing food preferences and nutritional behavior. Odorants interact with G-protein coupled receptors (GPCRs), encoded by about 400 odorant receptor (OR) genes [3–5]. At least 270 of these appear to be expressed in the cilia of olfactory sensory neurons (OSNs) within the main olfactory epithelium of the nasal cavity [6]. Odor coding supposedly is achieved in a combinatorial way—ORs are mainly broadly tuned and one odorant may activate multiple ORs [7–10].

Humans can distinguish between some enantiomeric odorants, suggesting enantiomer-specific ORs [11, 12]. The ability to discriminate between enantiomeric odorants is not a general phenomenon in primates, but probably limited to certain substances [13, 14], e.g., carvone, a KFO present in caraway, dill, or spearmint. Carvone comprises enantiomers with different odor qualities, with (*R*)-(-)-carvone or (*S*)-(+) -carvone displaying a spearmint-like or a caraway-like character, respectively. 8% of the population are anosmic for the spearmint KFO (*R*)-(-)-carvone [15]. However, the mechanisms underlying an enantiospecific or enantioselective activation of ORs are yet unclear.

For ORs, a specific interaction of single odorants with certain amino acid motifs, or single amino acid positions constituting an odorant binding pocket within the transmembrane region of ORs, has been postulated by several in silico studies, comprising sequence alignments, receptor homology modeling, and odorant docking [16–21]. Beyond that, a few studies have put in silico-derived models to the test, by combining site-directed mutagenesis and functional expression of wild-type and mutant receptors in cell systems, e.g., for the human OR1A1 and OR1A2 ((*S*)-(-)-citronellol, (*S*)-(-)-citronellal) [22], murine Olfr544 (alias MOR42-3, Ors6; variety of dicarboxylic acids) [23], murine Olfr73 (alias mOR-EG; eugenol) [24, 25], human OR2AG1 (amylbutyrate, isoamylbenzoate) [26], murine Olfr1509 (alias MOR244-3, ((methylthio)methanethiol) [27], murine Olfr124 (alias MOR256-3; allyl phenyl acetate, benzyl acetate, coumarin, (-)-carvone, 1-octanol) [16], and human OR2T11 (*t*-butyl mercaptan) [28]. These studies consistently identified odorant-interacting amino acid positions within certain transmembrane helices (TMH) or an extracellular loop (ECL) of ORs, mostly in TMH2-7 and ECL2.

ORs in olfactory sensory neurons typically operate by activating a biochemical signaling cascade, resulting in an increase of intracellular cyclic adenosine monophosphate (cAMP) [29–33]. Odorant-induced activity of recombinant ORs in test cell systems and accompanying changes in intracellular cAMP may be monitored by a variety of methods [7, 34–38]. Similar to but different from the well-established HEK-293-based luminescence static endpoint assay described by Zhuang and Matsunami [38], we

monitored cAMP-induced chemiluminescence in an HEK-293 cell-based, dynamic online GloSensor® assay [7, 39, 40], employing a genetically modified, cAMP-sensitive luciferase [41]. By this method, we tested an entire human OR repertoire with the (*R*)-(-)- or (*S*)-(+) -carvone enantiomers, and recently demonstrated carvone enantiomer-specific OR activation patterns, with OR1A1 being activated by both enantiomers, but displaying a selectivity for (*R*)-(-)-carvone over (*S*)-(+) -carvone [39, 40].

Here, we elucidate in detail an enantioselective carvone binding site in human OR1A1, which has been proposed by several groups independently to respond to both (*R*)-(-)-carvone [7, 39, 42] and (*S*)-(+) -carvone [7, 39, 42–44], as well as to several other compounds [7, 22, 40, 45]. We performed homology modeling, in silico docking studies, SNP analysis, site-directed mutagenesis, and functional expression of mutant receptors, orthologs of OR1A1, as well as its closest human homolog, OR1A2.

Materials and methods

Molecular cloning of human OR1A1, OR1A2, bovine OR1A1, and murine Olfr43

The protein-coding region (NCBI reference sequence, see Tab S1) of human OR1A1, OR1A2, bovine OR1A1, and murine Olfr43 was amplified from human, bovine, or murine genomic DNA with gene-specific primers (Tab S2) by polymerase chain reaction (PCR). We purified human genomic DNA from cell culture cells and bovine genomic DNA from beef meat using the blood and tissue kit (Qiagen, Hilden, Germany). Murine genomic DNA was obtained from BioChain Institute Inc., Newark, USA. PCR reactions (final volume: 50 µl) were performed in a C-1000 thermocycler (Bio-Rad, München, Germany) with 150 ng of respective genomic DNA, 0.5 µl phusion hot start DNA-polymerase (Thermo Scientific, Waltham, USA), 2.5 mM dNTPs (Promega, Madison, USA), 1.5 µl DMSO (Promega, Madison, USA), and 0.5 µM of each primer using the following protocol: denaturation (98 °C, 3 min), ten cycles containing denaturation (98 °C, 30 s), annealing (start 66 °C, 30 s, with –1 °C increment each cycle), extension (72 °C, 2 min), 30 cycles containing denaturation (98 °C, 30 s), annealing (58 °C, 30 s), extension (72 °C, 2 min), and final elongation (72 °C, 10 min). The control PCR reaction was without genomic DNA. PCR products were purified (gel extraction kit, Qiagen, Hilden, Germany), digested either *Eco*R1/*Not*1 or *Mfe*I/*Not*1 (Tab S2) and ligated (T4 DNA ligase, Promega, Madison, USA) into pI2-dk (39aa rho-tag) (aa, amino acids) [35, 46], which provides the first 39 amino acids of the bovine rhodopsin as an N-terminal tag for all full-length OR. *Eco*R1 and *Not*1

were from Promega (Madison, USA), and *Mfe1* from New England BioLabs (Ipswich, USA). All plasmid-DNAs were transformed by heat shock in competent *E. coli* (XL1-blue, Agilent Technologies, Santa Clara, USA) and purified with pure yield plasmid midiprep kit (Promega, Madison, USA). Plasmid-DNA concentrations were determined with Nanodrop 2000 (Thermo Fisher Scientific, Waltham, USA).

PCR-based site-directed mutagenesis

The human OR1A1, bovine btOR1A1, and murine Olfr43 receptor variants as well as the chimpanzee PTOR1A1 were generated by PCR-based two-step site-directed mutagenesis. Gene-specific primers carrying the nucleotides of interest (mutation-primer) as well as the vector-internal (dk-231), or in the case of OR1A1, a gene-specific (344) forward primer and a vector-internal (dk-232a) reverse primer were used (Tab S2–S6). The forward and reverse mutation-primers were designed to overlap. One PCR reaction was performed with the forward vector-internal (or in the case of OR1A1 with the gene-specific primer 344) and the respective reverse mutation-primer, and another PCR with the respective forward mutation-primer and the reverse vector-internal primer using the protocol as described above. The two purified PCR products were used as template for the second PCR. Here, the two templates were first annealed using the following protocol: denaturation (98 °C, 3 min), ten cycles containing denaturation (98 °C, 30 s), annealing (start 58 °C, 30 s), and extension (72 °C, 2 min). Then, the two vector-internal primers dk-231 and dk-232a (or in the case of OR1A1, 344 and dk-232a) were added, and the PCR was performed as described above. All following steps containing digest, ligation, and transformation were performed as described above.

Sequencing

All subcloned wild type (wt) and mutated OR coding region amplicons were verified by Sanger sequencing (Eurofins Genomics, Ebersberg, Germany). The reference sequence receptors were always referred to as wild type. All mutated ORs were named with the amino acid exchange at the respective position (e.g. OR1A1 G₁₀₈A).

Cell culture

HEK-293 cells (a human embryonic kidney cell line) (Graham et al., 1977) were cultivated in Dulbecco's modified eagle medium (DMEM: w 3.7 g/L NaHCO₃, w 4.5 g/L D-glucose, w/o L-glutamine, w/o Na-pyruvate) supplemented with 10% fetal bovine serum (FBS superior), 2 mM L-glutamine, 100 units/mL penicillin, and 100 µg/

mL streptomycin in 10 cm cell culture dishes at 37 °C, 5% CO₂, and 100% humidity. Cell culture medium and all supplements were obtained from Biochrom, Berlin, Germany.

Transfection

One day before transfection, HEK-293 cells were transferred with a density of 12000 cells per well in white 96-well plates (Nunc, Roskilde, Denmark). The transfection was done by the cationic lipid-transfection method (Lipofectamine 2000, Life Technologies, Carlsbad, USA), using 100 ng OR plasmid-DNA, 50 ng olfactory G-protein Gaolf [46, 47], 50 ng RTP1S [45], 50 ng Gy13 [48], and 50 ng genetically modified cAMP-luciferase pGloSensor™-22F [41] (Promega, Madison, USA) each. As a control, transfection of an empty vector-plasmid (mock) was performed. Each transfection was done in triplicates on the same 96-well plate and was repeated three times in independent experiments. The cells were taken into experiment 42 h post-transfection.

cAMP luminescence assay

Transfected HEK-293 cells were transferred into physiological salt buffer (pH 7.5) containing 140 mM NaCl, 10 mM HEPES, 5 mM KCl, 1 mM CaCl₂, 10 mM glucose, and 2% D-luciferin (beetle) monosodium salt (Promega, Madison, USA). The cells were incubated in D-luciferin supplemented buffer at room temperature for 1 h in the dark. This was necessary for the uptake of D-luciferin into the cells, which is required as a substrate for the luminescence reaction. After this incubation, basal luminescence signal readout (three consecutive data points) was recorded with GloMax®-MULTI⁺ detection system (Promega, Madison, USA) before odorant application. For each well, luminescence was recorded in 63 s intervals. Thereafter, the corresponding odorants ((R)-(-)-carvone and (S)-(+) -carvone) which were serially diluted in physiological salt buffer were pipetted to the cells. The carvone stock solutions were prepared in dimethyl sulfoxide (DMSO) and diluted 1:1000 in physiological salt buffer, resulting in a final concentration of 0.1% DMSO on the cells. After adding the odorants to the cells, a second readout (three consecutive data points) was recorded after reaching maximum receptor stimulation (4 min after odorant addition). This luminescence assay allows a real-time signal transduction measurement of changes in intracellular cAMP, which reaches a maximum within less than 5 min after receptor stimulation. The cells were stimulated only once with the corresponding odorant. No washout experiments were performed. Application of different

odorants or different concentrations of the same odorant to the same receptor need different transfections.

Data analysis of cAMP luminescence measurements

The raw luminescence data obtained from the GloMax®-MULTI⁺ detection system were converted to an excel document using Instinct Software (Promega, Madison, USA). Three consecutive data point values before (base level) and after odorant addition were averaged, respectively, and the corresponding baseline was subtracted from each signal. Concentration–response curves were performed in three independent experiments in triplicates. Concentration–response relations were obtained by normalizing the baseline-corrected data to maximum of the corresponding reference OR, which was in most cases the human OR1A1 wild type with (*R*)(–)-carvone (therefore, see the respective figure legends). The respective data from the vector-plasmid transfection (mock) were subtracted. EC₅₀ values (half maximal effective concentration) were derived from fitting the function $f(x) = 1/(1 + (\text{EC}_{50}/x)^h)$ to the data by non-linear regression (SigmaPlot 10.0, Systat Software), where h = Hill coefficient.

Phylogenetic analysis

For sequence comparisons and calculation of amino acid identities of human OR1A1, human OR1A2, chimpanzee PTOR1A1, bovine btOR1A1, and murine Olfr43, we used CLC Main Workbench 6.5.

We used the same software to perform the ClustalW alignment of the transmembrane regions (TMH) 1–7 and the extracellular loop (ECL) 2 of human OR1A1 and 38 homolog receptors (Tab S1). We created sequence logos using WebLogo 2.8.2 [49, 50]. The localization of the TMHs of human OR1A1 was taken from HORDE [51], and those of its homologs were obtained by their alignment with human OR1A1.

Homology modeling and docking

The homology models for the human OR1A1 and the murine Olfr43 were created based on automated template selection of the updated Sequence-Structure-Feature-Extractor database (SSFE [52–54]) version. For each helix, we chose a separate template based on the existing sequence features. For both models, the template selection was as follows: TMH1—human M2 muscarinic acetylcholine receptor (PDB ID: 3UON), TMH2 and TMH4—human dopamine D3 receptor (PDB ID: 3PBL), TMH3 and TMH7—human adenosine receptor A2a (PDB ID: 4EIY), TMH5—squid rhodopsin (PDB ID: 2Z73), TMH6—bovine rhodopsin (PDB ID: 1U19), and helix8—human

sphingosine 1-phosphate receptor 1. Due to special proline patterns Pro^{6,54} and Pro^{7,46} (nomenclature of positions according to Ballesteros and Weinstein [55]) of diverse ORs including OR1A1 (Fig. S1) that are not present in any of the current available structural templates, we modified TMH6 and TMH7 manually, by matching the sequence and proline patterns from other protein structure templates. For TMH6, we used corresponding fragments of peptide transporter POT (PDB ID: 4IKV, residues 164–173), and for TMH7, we used the multidrug resistant transporter of *E. coli* (PDB ID: 2GFP, residues 145–149). For an overview of the used templates, see Fig. S2 and Tab S7. As modeling software, we used Sybyl-X 2.1.1 (Certara, USA) and Maestro 11.0 (Schrödinger LLC, USA). The resulting modified proline kink in TMH6 and an additional kink in TMH7 caused a smaller binding pocket, at least between TMH1-3 and 7.

The identification of all possible conformational states of the ligands (*R*)(–)-carvone and (*S*)(+)-carvone (Conformational Search, FFAmber12:EHT), as well as the docking (Induced Fit, Default Settings, FFAmber12:EHT), was performed using the Molecular Operating Environment (MOE2016.0801—Chemical Computing Group Inc., Canada). All additional minor manual correction and the minimization were performed with Sybyl-X 2.1.1 (Certara, USA).

Results

Carvone enantioselective and enantiospecific OR1A1 homologs

We first studied whether the selectivity of OR1A1 for (*R*)(–)-carvone over (*S*)(+)-carvone [40] is an evolutionary conserved function, or rather a human-specific feature of OR1A1. Therefore, we investigated human odorant receptor OR1A1 and its homologs with amino acid identities of >80%, for instance, human OR1A2 (84%), chimpanzee PTOR1A1 (99%), bovine btOR1A1 (86%), and murine Olfr43 (83%) (Fig. 1a, for accession numbers of reference sequences see Tab S1). Concentration–response relations of transiently transfected OR1A1 in HEK-293 cells, and subsequent monitoring of cAMP luminescence with the dynamic online GloSensor® assay, showed selectivity of OR1A1 for the minty ((*R*)(–) carvone) over the caraway ((*S*)(+)-carvone) odor (Fig. 1b). Murine Olfr43 appeared to be specific for the (–)-enantiomer (Fig. 1f), whereas btOR1A1 appeared to be extremely selective for the (–)-enantiomer over the (+)-enantiomer (Fig. 1e), at least up to a concentration of 2 mM. In contrast, human OR1A2 responded neither to (*R*)(–)-carvone, nor to (*S*)(+)-carvone. Moreover, mutations in OR1A2 of

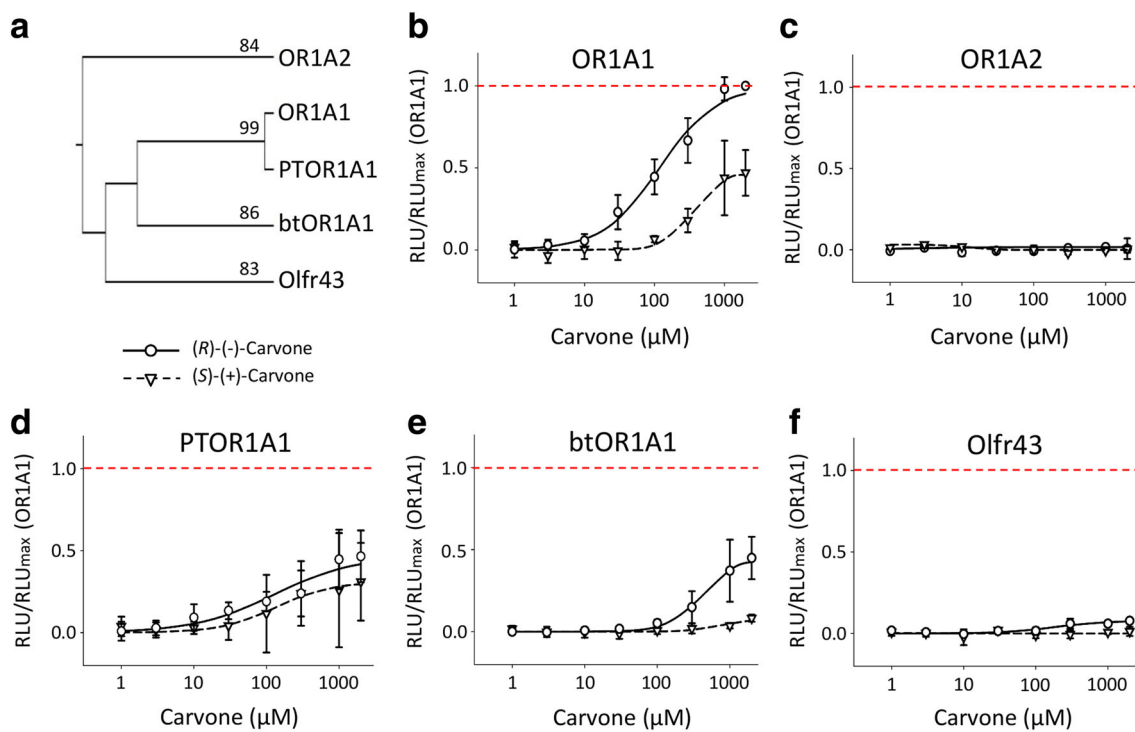


Fig. 1 Enantiomer-selective and enantiomer-specific homolog carvone ORs. **a** Phylogenetic tree of human OR1A1 and homologs. The numbers represent the amino acid identities of respective homologs to human OR1A1. Concentration–response relations of (R)-(-)-carvone and (S)-(+)-carvone for **b** OR1A1 (*Homo sapiens*), **c** OR1A2 (*Homo sapiens*), **d** PTOR1A1 (*Pan troglodytes*), **e** btOR1A1 (*Bos taurus*),

and **f** Olfr43 (*Mus musculus*). Shown are mean \pm SD of $n = 3\text{--}5$. Mock control was subtracted. Data were normalized to the OR1A1 maximum amplitude. The red dashed line indicates the normalization level. RLU relative luminescent unit. Subpanels **b** and **d** were taken with permission from [40]

amino acids constituting a putative binding site [20] to the corresponding OR1A1 amino acids did not result in an OR1A2 gain-of-function variant for neither of the carvone enantiomers (Fig. S3). The closest related ortholog, PTOR1A1, responded non-selectively to both carvone enantiomers (Fig. 1d).

Odorant binding pocket-associated amino acid mutations convert carvone enantioselectivity to enantiospecificity and vice versa in human OR1A1 and its murine ortholog Olfr43

In an in silico approach to elucidate odorant binding within ORs, Pilpel and Lancet (1999) by comparing ~ 200 amino acid sequences of paralogous ORs and other GPCRs determined 17 hypervariable amino acid positions constituting a putative odorant binding site [56]. In an extended approach comparing more than 1400 human and murine OR orthologs and paralogs, in 2004, Man et al. determined 22 amino acid positions, which constitute a putative, generalized, and conserved odorant binding pocket within OR orthologs [20]. To identify amino acid positions in two OR orthologs that are necessary for an enantioselective or even enantiospecific interaction with odorants, we compared

carvone enantioselective human OR1A1 with carvone enantiospecific murine Olfr43.

Despite an overall amino acid identity of 84%, Olfr43 unlike OR1A1 did not respond to (S)-(+)-carvone, and showed only a small signal response to (R)-(-)-carvone (Fig. 2a, b). Sequence alignment of OR1A1 and Olfr43 revealed three amino acid differences within those 22 amino acid positions predicted to constitute a conserved odorant binding pocket, located at positions 108^{3,36} (TMH3), 152^{4,53} (TMH4), and 205^{5,46} (TMH5) (Fig. 2c; Fig. S4). Apart from the absolute position number, the Ballesteros–Weinstein nomenclature [55] is also given for comparability of TMH positions between OR1A1 and Olfr43 and with other GPCRs. By introducing mutual exchanges at exactly these positions within OR1A1 and its murine ortholog Olfr43, we then tested whether we could convert OR1A1 into a carvone enantiospecific receptor and Olfr43 into a carvone enantioselective receptor (Fig. 2d–n). The mutual exchange of G₁₀₈A/G₁₅₂A in OR1A1, and vice versa A₁₀₈G/A₁₅₂G in Olfr43, resulted in inverted effects, (1) in a reduced (R)-(-)-carvone function and in a complete loss of (S)-(+)-carvone function for OR1A1 (Fig. 2d, f; Tab S8), but (2) in a (R)-(-)-carvone gain-of-function for Olfr43 (Fig. 2e, k; Tab S9). In OR1A1, the exchange of

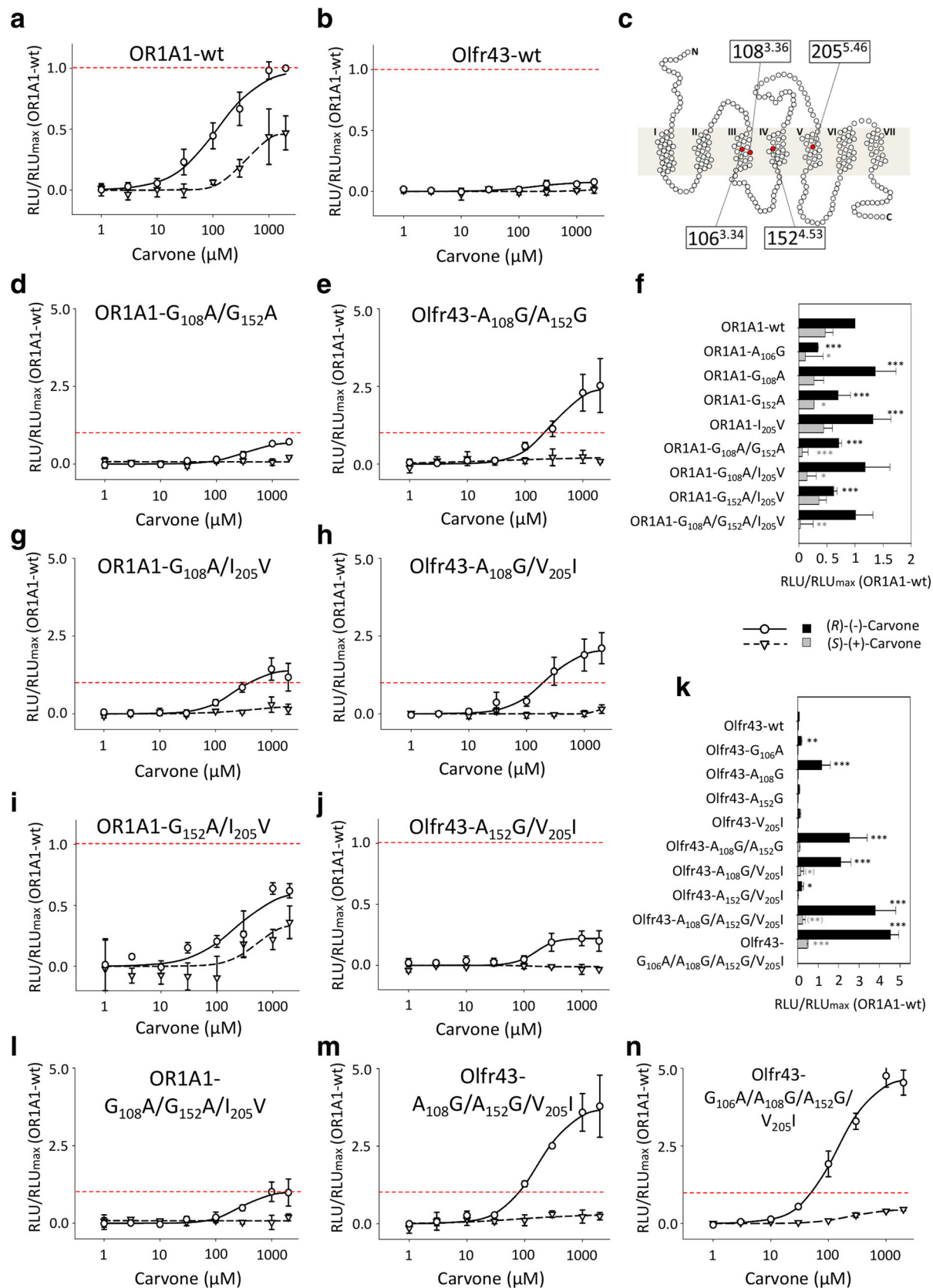


Fig. 2 Impact of amino acid residues within a predicted putative binding site of human OR1A1 and its murine ortholog Olfr43 on (*R*)-(−)-carvone and (*S*)-(+) -carvone function. Concentration-response relations of (*R*)-(−)-carvone and (*S*)-(+) -carvone for **a** OR1A1-wt (wild type, *H. sapiens*) and **b** Olfr43-wt (wild type, *M. musculus*). **c** Schematic snake diagram with localization of mutated amino acid positions within OR1A1 and Olfr43. **d, e** Mutual exchange of amino acids at positions 108^{3,36} and 152^{4,53}. **f** Quantification of amplitudes of OR1A1 mutant receptors. **g, h** Mutual exchange of amino acids at positions 108^{3,36} and 205^{5,46}. **i, j** Mutual exchange of amino acids at positions 152^{4,53} and 205^{5,46}. **k** Quantification of amplitudes of Olfr43 mutant receptors. **l, m** Mutual exchange of amino acids at positions 108^{3,36}, 152^{4,53}, and 205^{5,46}. **n** Replacement of the amino acids at positions 106^{3,34}, 108^{3,36}, 152^{4,53}, and 205^{5,46} in Olfr43. Shown are mean ± SD of $n = 3\text{--}5$. Mock control was subtracted. Data were normalized to the maximum response of OR1A1-wt with (*R*)-(−)-carvone. The red dashed line indicates the normalization level. RLU relative luminescent unit. *Significant differences ($p < 0.05$) of the (*R*)-(−)-carvone (black asterisks) and (*S*)-(+) -carvone (grey asterisks) responses between wild type (wt) and mutant receptors. Concentration-response relations for single amino acid mutations in OR1A1 and Olfr43 are given in Supplemental Fig S5. For didactic reasons, we included the panels of OR1A1-wt and Olfr43-wt from Fig. 1b, f

two amino acids at positions 108^{3,36} and 205^{5,46} from human to murine, OR1A1-G₁₀₈A/I₂₀₅V, caused a shift in EC₅₀, due to a loss of sensitivity of OR1A1 for (*R*)-(−)-carvone, and a reduced (*S*)-(+) -carvone function for OR1A1 (Fig. 2g, f; Tab S8). Vice versa, the double mutant Olfr43-A₁₀₈G/V₂₀₅I resulted in a gain of (*R*)-(−)-carvone function (Fig. 2h, k; Tab S9). Combining positions 152^{4,53} and 205^{5,46}, the double mutant OR1A1-G₁₅₂A/I₂₀₅V displayed a reduced function for both carvone enantiomers, with respect to both EC₅₀ and efficacy (Fig. 2i, f; Tab S8). In contrast, Olfr43-A₁₅₂G/V₂₀₅I displayed an increased (*R*)-(−)-carvone function as compared to the wild type, albeit with lower efficacies when compared to Olfr43-A₁₀₈G/A₁₅₂G and Olfr43-A₁₀₈G/V₂₀₅I (Fig. 2j, k; Tab S9).

As an important result from all experiments with single and double mutants, so far, we learned that position 108^{3,36} itself is critical for a (*S*)-(+) -carvone function in OR1A1, and for a (*R*)-(−)-carvone function in Olfr43. Indeed, in our hands, just the single mutations Olfr43-A₁₀₈G and OR1A1-G₁₀₈A enabled a gain of (*R*)-(−)-carvone function and a loss of (*S*)-(+) -carvone function, respectively (Fig. 2f, k; Fig S5d; concentration-response curves of all single amino acid mutations within OR1A1 and Olfr43 are given in Fig S5).

Finally, an exchange of all three variable amino acids between OR1A1 and its ortholog Olfr43 at positions 108^{3,36}, 152^{4,53}, and 205^{5,46} rendered OR1A1-G₁₀₈A/G₁₅₂A/V₂₀₅I an enantiomer-specific receptor for (*R*)-(−)-carvone, with the same efficacy as OR1A1-wt, and, similar to Olfr43, with no (*S*)-(+) -carvone function (Fig. 2l, f; Tab S8).

Vice versa, the triple mutant Olfr43-A₁₀₈G/A₁₅₂G/V₂₀₅I displayed an about threefold increase in (*R*)-(−)-carvone function, as compared to Olfr43-A₁₀₈G, however, with only a minimal gain of (*S*)-(+) -carvone function (Fig. 2m, k; Fig S5i). Since position 108^{3,36} proved crucial for a (*S*)-(+) -carvone function in OR1A1, we decided to mutually exchange amino acids at position 106^{3,34} as well, which is also different in both receptors (OR1A1-Ala106, Olfr43-Gly106), and which is in close vicinity to position 108^{3,36}. Furthermore, Ala106 is affected by a non-synonymous single-nucleotide polymorphism (SNP) in OR1A1 (A₁₀₆T), but with a minor allele frequency <1 [57]. Moreover, sequencing different murine Olfr43 variants revealed G₁₀₆S as frequently occurring mutation (data not shown).

Consequently, we changed the amino acid at position 106^{3,34} in Olfr43 from murine to human, and found that finally, the quadruple mutant Olfr43-G₁₀₆A/A₁₀₈G/A₁₅₂G/V₂₀₅I displayed a gain of (*S*)-(+) -carvone function (Fig. 2n; Fig S5j), with a similar EC₅₀ and efficacy as OR1A1-wt. This mutant was carvone enantioselective, and had a similar EC₅₀, but a 4.5-fold increased efficacy for (*R*)-(−)-carvone as compared to the OR1A1-wt (Fig. 2n; Tab S9).

Homology models and ligand docking suggest different binding modes of carvone enantiomers within the binding pocket of OR orthologs

Mutual exchange of amino acid positions 106^{3,34}, 108^{3,36}, 152^{4,53}, and 205^{5,46} from human to murine and vice versa so far demonstrated the successful back and forth conversion of OR orthologs from being selective or specific for carvone enantiomers, thus suggesting that these four amino acid positions are involved in constituting a carvone enantiomer binding pocket in human OR1A1 and murine Olfr43. We, therefore, set out to establish TMH homology models and carvone enantiomer docking for both receptors, first to explain our experimental results, and second to propose further amino acid positions to refine a carvone enantioselective or enantiospecific binding pocket, in OR1A1 or Olfr43, respectively.

However, model building of ORs is a challenge, since the proline patterns in TMH6 and TMH7 of OR1A1 and the murine Olfr43 differ clearly from that in GPCR families A, B, and C (sequence: Fig S2), and thus, OR conformations of TMH6 and 7 are very likely different from currently existing GPCR crystal structures. Therefore, we not only used an updated multi-template SSFE approach (<http://www.ssfa-7tmr.de/ssfe2>) [52, 54] using different TMH fragment templates of best matching sequence fingerprint patterns for each transmembrane helix separately (see methods, Fig S2, and Tab S7), we also adjusted TMH6 and TMH7 additionally. The highly

conserved Pro^{6,50} in the middle of TMH6, which causes a pronounced kink in TMH6 in class A GPCRs, is lacking in the considered ORs. Instead, both human and murine receptors exhibit a proline (Pro261^{6,54}) located in a different position at TMH6. Apart from the highly conserved Pro285^{7,50} in TMH7, an additional proline is present in position Pro281^{7,46} in both OR1A1 and Olfr43. None of the currently available GPCR crystal structures provides a template that matches these specific patterns in TMH6 and TMH7, and no crystal structures exist for ORs, yet. Using matching proline patterns from other protein structures (see “Materials and methods”; Tab S7), our manual adjustments of TMH6 and TMH7 modified the kink in TMH6, and newly introduced a kink in TMH7. Compared to the generic transmembrane ligand binding site known for GPCR class A [58], the adjusted kinks of TMH6 and TMH7 reduced the size of the transmembrane odorant binding site in the OR1A1 model considerably. Our adjustment especially reduced the interior space between TMH1, 2, and 3, which, in our OR1A1 model, is almost occluded by aromatic residues (Phe73^{2,53}, Phe250^{6,43}, and Phe276^{7,41}) (Fig. 6a, b). This is consistent with odorant ligands, which are almost all of small size, and with hydrophobic properties. As a result, both OR models with manually adjusted GPCR templates showed ligand interactions in our docking studies that are consistent with our mutational studies (Figs. 3, 4, 5, 6). In contrast, the initial models based on unaltered single GPCR templates provided a high number of false positive docking results (data not shown).

Molecular determinants in TMH3, TMH4, and TMH5 for carvone interactions in the OR1A1 and Olfr43 models

Our models of human OR1A1 and murine Olfr43 now indicate that two of the mutation-sensitive residues at positions 108^{3,36} (TMH3) and 205^{5,46} (TMH5) are lining the binding pocket (grey surface in Fig. 3) and interact directly with the carvone enantiomers (Fig. 3). However, two other mutation-sensitive residues at positions 106^{3,34}, (TMH3) and 152^{4,53} (TMH4) are not directly interacting with the carvones. Both positions, 106^{3,34} and 152^{4,53}, are very close to each other in space and form a tight interacting interface between TMH3 and TMH4 (Figs. 3, 5a).

Asn109^{3,37} is necessary for the detection of both carvone enantiomers

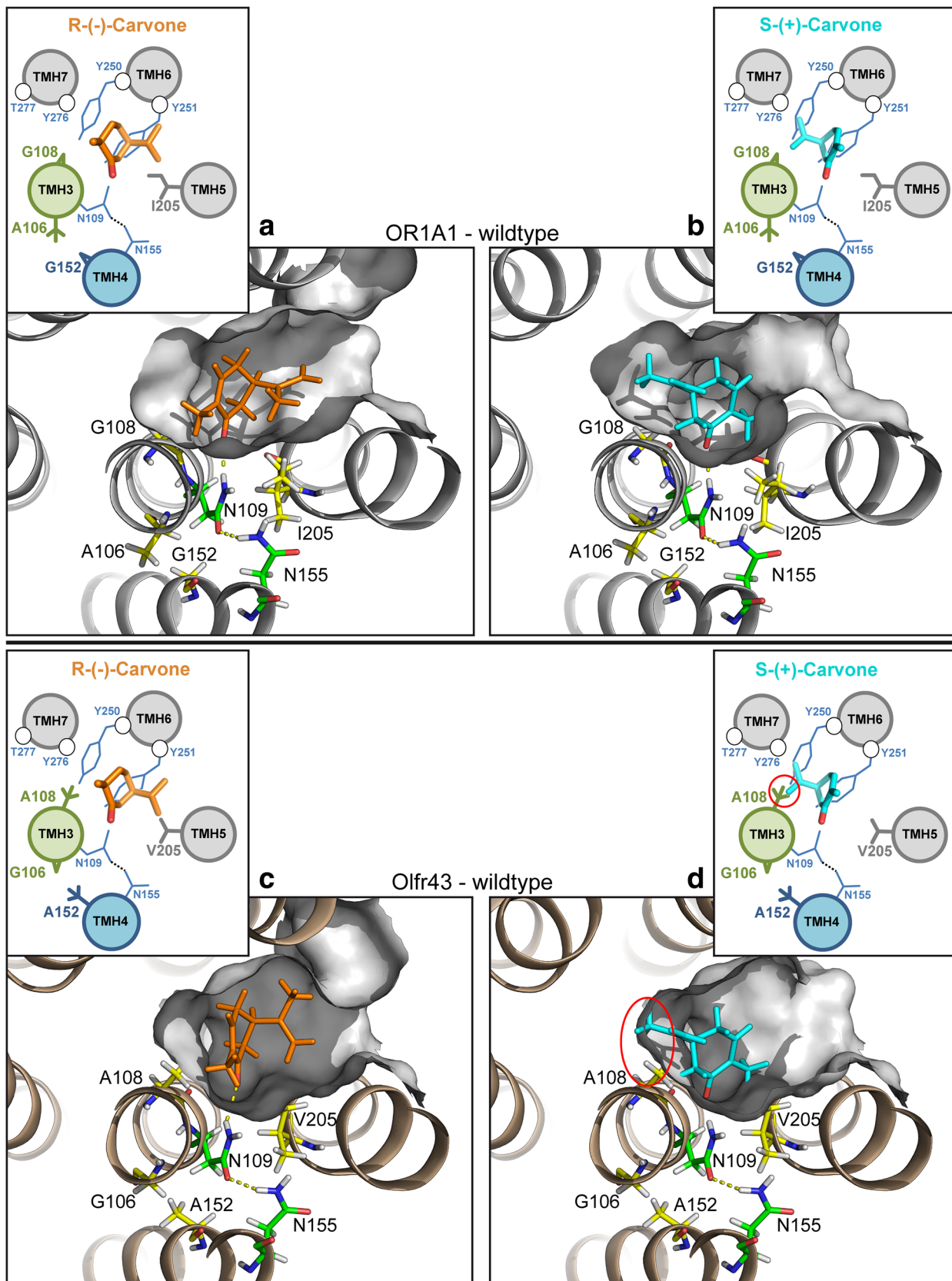
Docking of both carvones into our new OR models points to the proton-donating NH₂ group of the conserved side chain Asn109^{3,37} at TMH3 as an essential interaction site

Fig. 3 Molecular models of differing ligand binding cavities for human OR1A1 (grey, **a**, **b**) and murine Olfr43 (sand, **c**, **d**) located between transmembrane helices TMH3–7 and the interaction with (*R*)(–)-carvone (orange) and (*S*)(+)-carvone (cyan). Simplified schemes are shown as insets. Residues defining the binding pocket (calculated grey surface) are shown as sticks (oxygen: red; nitrogen: blue). The small side chain of Gly108^{3,36} in OR1A1 provides at TMH3 an enlarged ligand binding pocket (grey surface) compared to Olfr43 where the slightly larger side chain of Ala108^{3,36} decreased the binding pocket at TMH3. (*R*)(–)-carvone (orange) and (*S*)(+)-carvone (cyan) are visualized including their hydrogens. The small 2-methyl and bulky 5-(1-methyl-ethenyl) moiety of the carvones is oriented vice versa within the binding pocket for the two enantiomeric conformations. Hydrogen bonds are indicated by dashed lines in yellow. The essential intermolecular hydrogen bond between the 1-ketone oxygen (red) of (*R*)(–)- and (*S*)(+)-carvone to the NH₂ group of Asn109^{3,37} at TMH3 can be established in OR1A1 by **a** (*R*)(–)-carvone and **b** (*S*)(+)-carvone, since the small Gly108^{3,36} side chain provides enough space interacting with both enantiomers. **c** Restricted binding pocket (due to Ala108^{3,36}) in Olfr43 allows only interaction with the small 2-methyl group of (*R*)(–)-carvone to form an H-bond to Asn109^{3,37}. **d** Binding of (*S*)(+)-carvone is prevented in Olfr43 due to sterical clashes with pocket borders restricted by Ala108^{3,36} and Val205^{5,46} (hindrance, red oval). This is indicated by a manual docking pose of (*S*)(+)-carvone (cyan), where the bulky 5-(1-methyl-ethenyl) and the 2-methyl moieties are protruding the calculated pocket surface (grey) and cannot properly establish the H-bond towards Asn109^{3,37}, which explains the diminished effect on Olfr43. Conserved/variant residues are colored in green/yellow

within the binding pocket of both receptors (Fig. 3). The proton-accepting ketone oxygen (marked red in Fig. 3) of (*R*)(–)- and (*S*)(+)-carvone is the driving counterpart forming the pivotal intermolecular hydrogen bond towards Asn109^{3,37}, which can be established in human OR1A1 by (*R*)(–)-carvone (Fig. 3a), as well as by (*S*)(+)-carvone (Fig. 3b) but in different orientations. Thus, the smaller 2-methyl and bulky 5-(1-methyl-ethenyl) moiety of the bound carvones is within the binding pocket oriented vice versa for the two enantiomeric conformations.

The importance of Asn109^{3,37} for carvone binding is further underlined by model-guided mutations (N₁₀₉D, N₁₅₅S) in OR1A1 (Fig. 5b, c). Replacement of the Asn109 in OR1A1-N₁₀₉D eliminates the amino carbonyl NH₂-group, and resulted in a complete loss-of-function for both carvone enantiomers (Fig. 5b; Tab S8), which is consistent with our interaction model (Figs. 3, 5a).

The model further indicates that the NH₂ orientation of Asn109^{3,37} into the binding pocket is stabilized by the conserved Asn155^{4,56} located at TMH4, which thus indirectly contributes to the carvone binding site by an H-bond interaction towards Asn109^{3,37} (Figs. 3, 5a). Consequently, OR1A1-N₁₅₅S showed a largely diminished (*R*)(–)-carvone function, with its (*S*)(+)-carvone function abolished (Fig. 5c; Tab S8), which is also consonant with our interaction model (Figs. 3, 5a).



The variant positions 108^{3,36}, together with 106^{3,34}, 152^{4,53}, and 205^{5,46} distinguish between (R)-(-)- and (S)-(+)-carvone

In OR1A1, the small side chain of Gly108^{3,36}—adjacent to Asn109^{3,37}—provides enough space to accommodate both carvone enantiomers, whereas slight enlargement by Ala108^{3,36} in murine Olfr43, combined with a slight difference in the position of TMH3, restricts the binding pocket and prevents an interaction with (S)-(+)-carvone due to steric hindrance with its bulky 5(1-methyl-ethenyl) moiety (Fig. 3d, red oval). To visualize this fact, a manual docking pose is given in Fig. 3d. As a result, the ketone oxygen of (S)-(+)-carvone cannot properly establish the essential H-bond with Asn109^{3,37} in Olfr43.

This particular H-bond interaction is consistent with our finding that changing glycine to the larger alanine at position 108 in OR1A1–G₁₀₈A resulted in a loss-of-function for (S)-(+)-carvone (Fig. 5d; Tab S8). Our model now explains why Olfr43 has no (S)-(+)-carvone function to begin with, and illuminates the loss of (S)-(+)-carvone function of chimeric double mutants of OR1A1, such as G₁₀₈A/G₁₅₂A (Fig. 2d; Tab S8) and G₁₀₈A/I₂₀₅V (Fig. 2g; Tab S8).

Likewise, the effect of an increased (R)-(-)-carvone function of the corresponding chimeric double mutations in Olfr43, such as A₁₀₈G/A₁₅₂G (Fig. 2e; Tab S9) and A₁₀₈G/V₂₀₅I (Fig. 2h; Tab S9), is explained by our model, suggesting a direct participation of positions 108^{3,36}, 152^{4,53}, and 205^{5,46} in the binding site.

The tight interacting TMH3/TMH4 interface, as comprised by the complementary variant positions Gly106^{3,34}/Ala152^{4,53} or Ala106^{3,34}/Gly152^{4,53}, in Olfr43 or OR1A1, respectively (Figs. 3, 5a), determines the spatial localization of the particular backbone of TMH3, but is not directly interacting with the binding site. Mutual vice versa mutations A₁₀₆G, G₁₅₂A in OR1A1 (Fig. 5f, g), and, respectively, in Olfr43 (Figs. 1f, k, 2f, 3; Tab S8) alter the interface and supposedly lead to steric effects between TMH3 and TMH4. Thereby, the spatial positions of Gly108^{3,36} and Asn109^{3,37} (TMH3) are altered, and thus indirectly influence the binding of the carvone enantiomers (Fig. 3a, c). Consequently, only the Gly108^{3,36}–Ala106^{3,34}–Gly152^{4,53} interplay of amino acid positions in TMH3–4, together with Ile205^{5,46} in TMH5, in the Olfr43 quadruple mutant G₁₀₆A/A₁₀₈G/A₁₅₂G/V₂₀₅I, is providing enough space also for the (S)-(+)-carvone enantiomer, thus enabling a gain of (S)-(+)-carvone function (Figs. 2n, 3b, d, 4b; Tab S9). The substitutions G₁₀₆A and A₁₅₂G alter the position of TMH3 in Olfr43–G₁₀₆A/A₁₀₈G/A₁₅₂G/V₂₀₅I compared to Olfr43-wt, enlarging the binding cavity indirectly, while substitution A₁₀₈G enlarges the binding cavity directly (Fig. 4). In combination with substitution V₂₀₅I, which affects the positioning of Asn109^{3,37}, the binding of (S)-(+)-carvone is now possible (Fig. 4b).

Conserved Y251^{6,44} and Y276^{7,41} at TMH6 and TMH7 line an extended hydrophobic carvone binding site in OR1A1

Beyond the variant amino acid positions 108^{3,36} and 205^{5,46}, and the conserved Asn109^{3,37}, which we identified as direct interaction partners for the carvones, so far (Figs. 2, 3), our binding site model of human OR1A1-wt further proposed direct, hydrophobic interactions of both carvone enantiomers with conserved amino acids Tyr251^{6,44} and Tyr276^{7,41} (Fig. 6a, b).

To put our model to the test, we performed site-directed mutagenesis of all proposed carvone-interacting amino acids in OR1A1, and compared the function of the mutants with the OR1A1-wt (Fig. 6c–i).

Eliminating the hydroxyl group of the tyrosines in OR1A1–Y₂₅₁F and OR1A1–Y₂₇₆F resulted in all cases in a diminished function for both carvone enantiomers (Fig. 6c, e; Tab S8). Eliminating the aromatic ring of the tyrosines by substitution to methionine in OR1A1–Y₂₅₁M and to leucine in OR1A1–Y₂₇₆L, however, resulted in both cases in a complete loss-of-function of these mutants (Fig. 6d, f; Tab S8). According to our model, among the hydrophobic aromatic cluster, residue Tyr250^{6,43} participates only marginally and indirectly in the carvone binding pocket (Fig. 6a, b). The OR1A1 model further indicates that an H-bond-mediated interaction with Asp111^{3,39} adjusts the side chain orientation towards TMH3 (Fig. 6g). We therefore tested whether eliminating the hydroxyl group in OR1A1–Y₂₅₀F or the carboxylic acid group in OR1A1–D₁₁₁A had a similar effect on the carvone function in OR1A1. Indeed, both mutants displayed an identical, enantiomer-specific phenotype, with a diminished (R)-(-)-carvone function, but a complete loss of (S)-(+)-carvone function (Fig. 6h, i; Tab S8), indicating that the H-bond got lost. This supports our hypothesis that the aromatic ring of Tyr250^{6,43} must be in the appropriate orientation towards TMH3, arranging the other aromatic residues Tyr251^{6,44} and Tyr276^{7,41} properly, especially to accommodate the bulky 5(1-methyl-ethenyl) moiety of (S)-(+)-carvone.

Identification of further amino acids in OR1A1 for a carvone enantioselective function by mutating the odorant binding pocket in the bovine ortholog receptor

OR1A1 and the ortholog bovine receptor btOR1A1 share an overall amino acid identity of 86%. As shown in Fig. 7, human OR1A1 is selective for (R)-(-)-carvone over (S)-(+)-carvone, whereas its bovine ortholog is largely selective for the (R)-(-)-enantiomer, albeit with a lower potency and efficacy than the human receptor (Fig. 7b, c; Fig S10). The amino acids identified in this study to

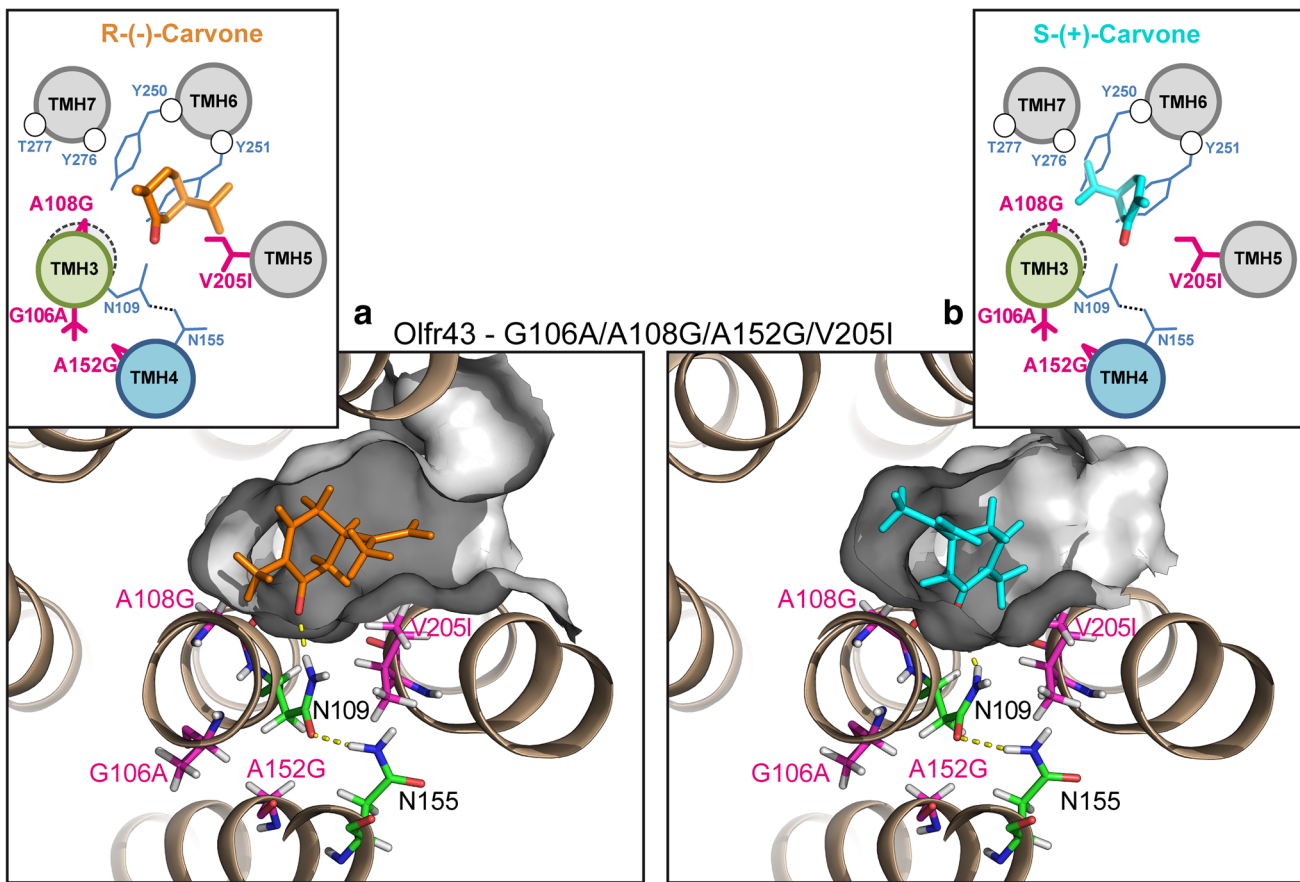


Fig. 4 Molecular models of the ligand binding cavity for the quadruple mutant Olfr43-G₁₀₆A/A₁₀₈G/A₁₅₂G/V₂₀₅I. Simplified schemes are shown as insets, the quadruple mutation changes the position of TMH3 (green circle) slightly compared to Olfr43-wt (dashed black circle). Residues defining the binding pocket (calculated grey surface) are shown as sticks (oxygen: red; nitrogen: blue)

constitute the carvone binding site in human OR1A1 and murine Olfr43 (Table 1) are identical between OR1A1 and btOR1A1, with the exception of amino acid position 205^{5,46} (Fig S4). Comparison of the 22 positions, predicted to contribute to a conserved odorant binding pocket [20], between OR1A1 and its *Bos taurus* ortholog, revealed three differences (I₁₀₅L, I₂₀₅V, and T₂₇₇I, from human to bovine, Fig. 7a; Fig S4). Two of them (I₁₀₅L and T₂₇₇I) did not correspond to the differences in the predicted binding pocket found in human OR1A1 and murine Olfr43. Whereas a difference at position 205^{5,46} (I₂₀₅V) can also be found in OR1A1 and Olfr43 (Fig. 7a, Fig S4, compared to Fig. 2c). We replaced these amino acids (single, double, and triple replacements) in the bovine receptor with the corresponding ones of human OR1A1 (Fig. 7d). Already the single mutant I₂₇₇T displayed a gain-of-function for both (R)-(−)-carvone and (S)-(+)-carvone, doubling the (R)-(−)-carvone efficacy (Fig. 7d, f; Tab S10). The btOR1A1 mutants containing threonine (Thr) instead of

(R)-(−)-carvone (orange) and (S)-(+)-carvone (cyan) are visualized including their hydrogens. Compared to Olfr43-wt, the position of TMH3 is slightly altered in Olfr43-G₁₀₆A/A₁₀₈G/A₁₅₂G/V₂₀₅I, which in combination with the shortening of side chain A₁₀₈G enlarges the binding cavity. These changes allow a better binding of **a** (R)-(−)-carvone (orange) and **b** enable binding of (S)-(+)-carvone (cyan)

isoleucine (Ile) at position 277 (btOR1A1-I₂₇₇T, btOR1A1-L₁₀₅I/I₂₇₇T, and btOR1A1-V₂₀₅I/I₂₇₇T) displayed a gain of (R)-(−)-carvone function, and, with the exception of btOR1A1-L₁₀₅I/I₂₇₇T, also had a gain of (S)-(+)-carvone function, as compared to btOR1A1-wt (Fig. 7d; Fig. S6).

Interestingly, an SNP (T₂₇₇M) may affect position 277^{7,42} in human OR1A1, with a minor allele frequency of 2.7% [57]. In our hands, OR1A1-T₂₇₇M, caused a largely diminished (R)-(−)-carvone function, and a complete loss of (S)-(+)-carvone function (Fig. 7e; Tab S8). Simultaneous exchange of all three amino acids from bovine to human rendered btOR1A1-L₁₀₅I/V₂₀₅I/I₂₇₇T a largely human OR1A1 wild type-like receptor, with almost the same efficacies for (R)-(−)-carvone and (S)-(+)-carvone, albeit with higher EC₅₀ values (Fig. 7c, red curves).

Thus, the triple mutant btOR1A1-L₁₀₅I/V₂₀₅I/I₂₇₇T installed a carvone enantioselective, human-like receptor, in contrast to the almost enantiospecific btOR1A1 wild-

Fig. 5 Indirect stabilization of the OR1A1 binding site. **a** View onto the interaction between TMH3 and TMH4 indicates an interaction of Ala106^{3,34} with Gly152^{4,53} and Asn109^{3,37} with Asn155^{4,56}. Changes in either Ala106^{3,34} or Gly152^{4,53} lead to steric effects between TMH3 and TMH4 and thereby influence the spatial positions of Gly108^{3,36} and Asn109^{3,37}. The side chain of Asn109^{3,37} is positioned through interaction with Asn155^{4,56}, and points into the binding pocket (Fig. 3). Decreased functional effects by the single mutations of **b** N₁₀₉D, **c** N₁₅₅S, **d** G₁₀₈A, **e** I₂₀₅V, **f** A₁₀₆G, and **g** G₁₅₂A support this model. Shown are mean \pm SD of $n = 3\text{--}5$. Mock control was subtracted. Data were normalized to the maximum response of OR1A1-wt (wild type) with (R)-(-)-carvone. The red dashed line indicates the normalization level. RLU relative luminescent unit. For didactic reasons, we included the panel of OR1A1-wt (wild type) from Fig. 1b in the background (grey) of each subpanel

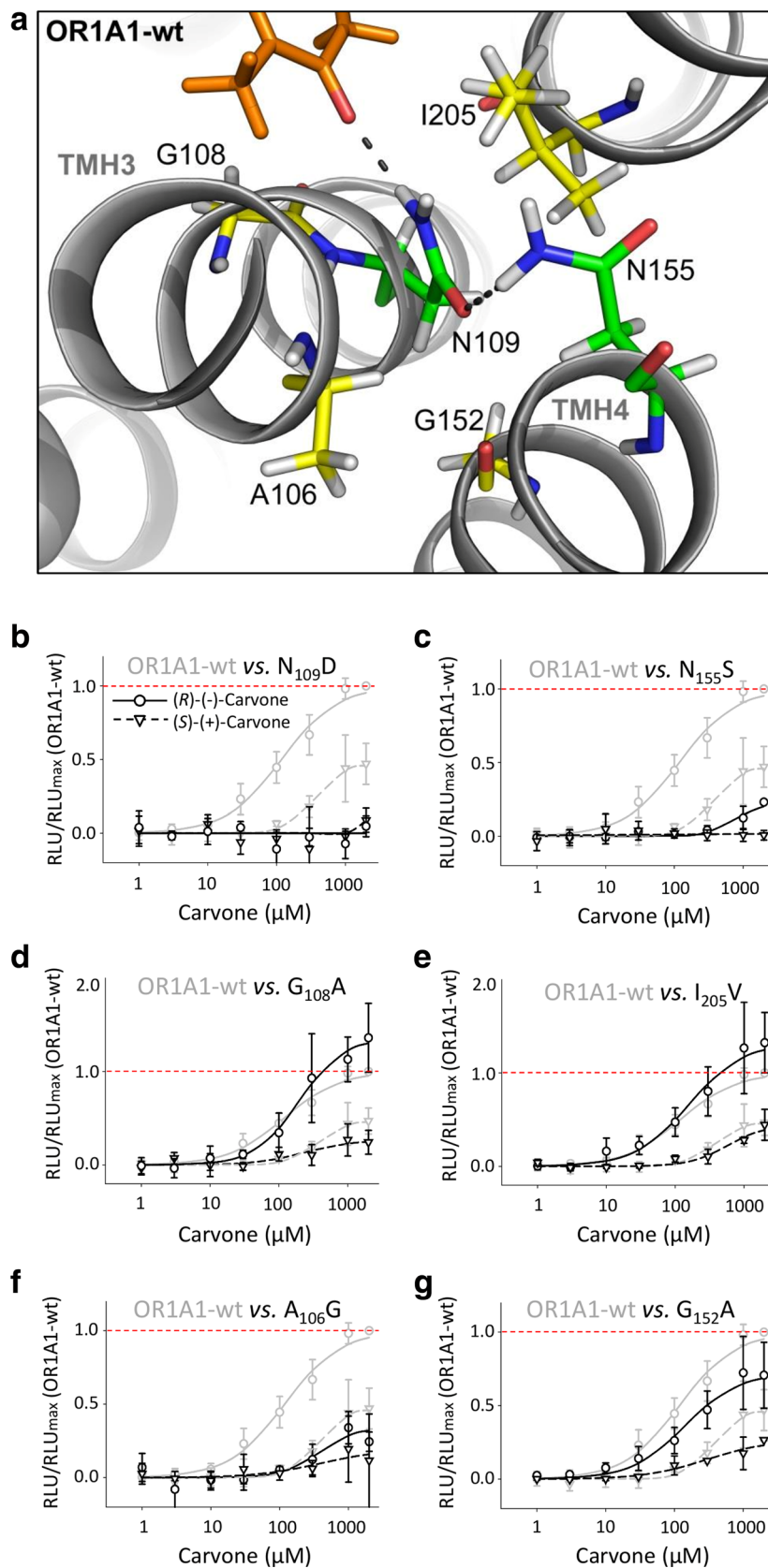
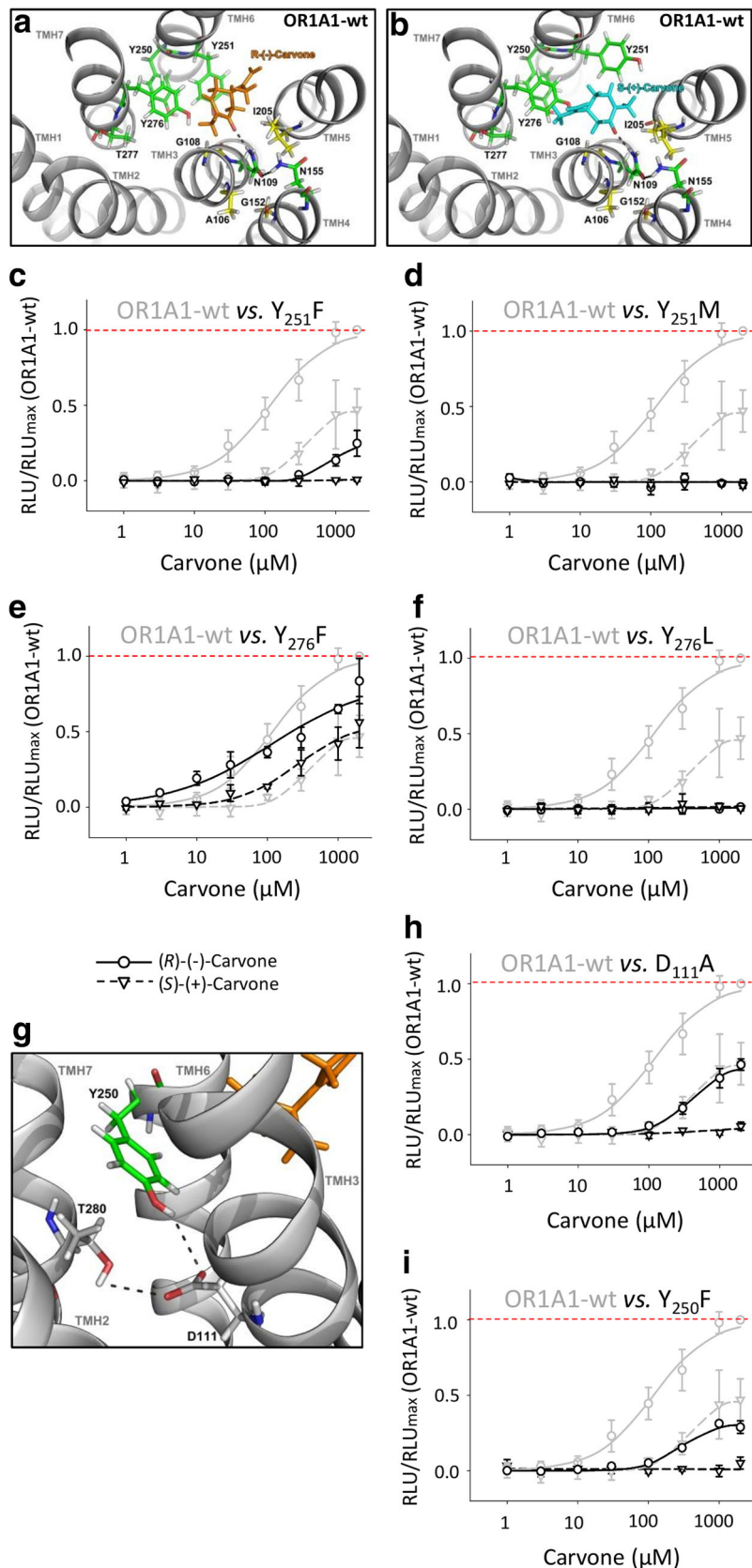


Fig. 6 Amino acids directly interacting with carvone within OR1A1 binding site. The OR1A1 binding site model for **a** (*R*)-(−)-carvone and **b** (*S*)-(+)-carvone shows the residues directly interacting with carvone: Ile205^{5,46}, Tyr251^{6,44}, and Tyr276^{7,41}. The single mutations of **c** Y₂₅₁F, **d** Y₂₅₁M, **e** Y₂₇₆F, and **f** Y₂₇₆L support this model. **g** View onto the interactions between TMH3, TMH6, and TMH7, which indicate an interaction of Tyr250^{6,43} with Asp111^{3,39}. The predicted H-bond interaction is directing the side chain orientation of Tyr250^{6,43}, which defines the binding site flanking (*R*)-(−)-carvone (orange) between TMH3 and TMH6. Decreased functional effects by single mutations at both sites **h** Asp111^{3,39} and **i** Tyr250^{6,43} support this model. Shown are mean \pm SD of $n = 3\text{--}5$. Mock control was subtracted. Data were normalized to the maximum response of OR1A1-wt (wild type) with (*R*)-(−)-carvone. The red dashed line indicates the normalization level. RLU relative luminescent unit. For didactic reasons, we included the panel of OR1A1-wt (wild type) from Fig. 1b in the background (grey) of each subpanel



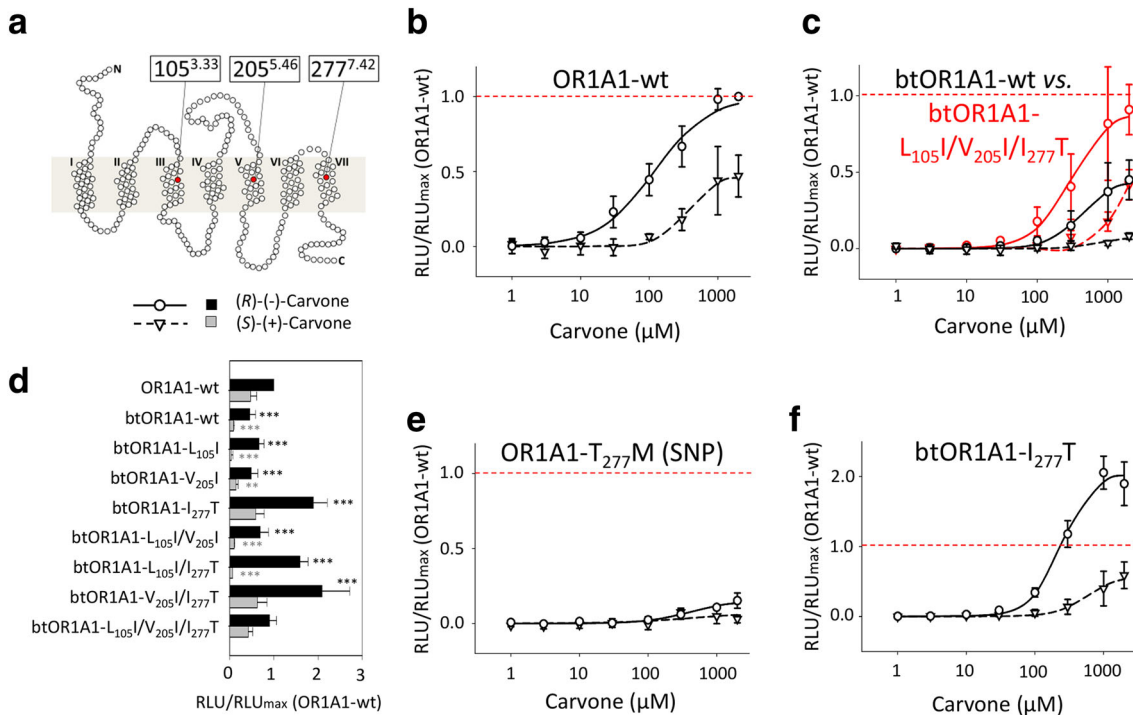


Fig. 7 Impact of amino acid residues within a predicted putative binding site of human OR1A1 and its ortholog btOR1A1 on (R)-(-)-carvone and (S)-(+) -carvone function. **a** Schematic snake diagram with localization of mutated amino acid positions within human and bovine OR1A1. Concentration-response relations of (R)-(-)-carvone and (S)-(+) -carvone for **b** OR1A1-wt (wild type, *H. sapiens*), and **c** btOR1A1-wt (wild type, *B. taurus*) with btOR1A1-L₁₀₅I/V₂₀₅I/I₂₇₇T (red curves). **d** Quantification of amplitudes of btOR1A1 mutant receptors. **e** Replacement of the amino acid at position 277^{7.42} from threonine (Thr) to methionine (Met) in human OR1A1 (SNP, single-nucleotide polymorphism). **f** Replacement of the amino acid at position 277^{7.42} from isoleucine (Ile) to threonine (Thr) in btOR1A1.

type receptor. Comparing the mutants btOR1A1-V₂₀₅I/I₂₇₇T and btOR1A1-L₁₀₅I/V₂₀₅I/I₂₇₇T further revealed for the latter a diminished potency for (S)-(+) -carvone (increase in EC₅₀), which may result from changing the leucine to isoleucine at position 105^{3.33} (Tab S10). Our OR1A1 model indicates that Thr277^{7.42} is adjacent to Tyr276^{7.41} and points towards TMH2. The small residue threonine touches the binding pocket marginally but does not influence it very strongly. However, a larger side chain like isoleucine or methionine may influence the pocket volume either directly or indirectly by pushing TMH2 and TMH7 apart.

In summary, our experiments emphasize the importance of position Ile205^{5.46}, and suggest at least one more amino acid position, Thr277^{7.42}, to be involved, presumably either slightly directly or indirectly, in constituting a carvone enantioselective binding pocket in OR1A1.

Table 1 summarizes the 11 amino acids which we identified so far, in accordance with our model and our mutational studies, to constitute the carvone binding site in

This mutant corresponds to human OR1A1. Shown are mean \pm SD of $n = 3-5$. Mock control was subtracted. Data were normalized to the maximum response of human OR1A1-wt (wild type) with (R)-(-)-carvone. The red dashed line indicates the normalization level. RLU relative luminescent unit. *Significant differences ($p < 0.05$) of the (R)-(-)-carvone (black asterisks) and (S)-(+) -carvone (grey asterisks) responses between wild-type (wt) and mutant receptors. Concentration response relations for further amino acid mutations in btOR1A1 are given in Fig S6. For didactic reasons, we included the panels of OR1A1-wt (wild type) and btOR1A1-wt (wild type) from Fig. 1b, e

human OR1A1. Of these, five (Gly108^{3.36}, Asn109^{3.37}, Ile205^{5.46}, Tyr251^{6.44}, and Tyr276^{7.41}) supposedly interact directly with the carvones, and another six (Ala106^{3.34}, Asp111^{3.39}, Gly152^{4.53}, Asn155^{4.56}, Tyr250^{6.43}, and Thr277^{7.42}), supposedly have an indirect effect stabilizing the appropriate conformation of the binding pocket.

The carvone binding pocket of OR1A1 is most highly conserved specifically among hominid orthologs

We investigated the conservation of amino acids at those positions, which we identified in this study so far to be involved, directly or indirectly, in constituting the carvone binding site in OR1A1, and those 22 amino acid positions, which Man et al. predicted to constitute a general odorant binding site [20]. We, therefore, performed an amino acid sequence alignment and established phylogenetic relationships for OR1A1 orthologs from 37 mammalian species (for details, see Tab S1, and Fig S7). Figure 8

Table 1 Amino acids constituting a carvone binding site in OR1A1 and Olfr43

AA-position within TMH segment ^a	Mutagenesis-validated carvone binding site positions		OR1A1 (Fig. 3a, b)		Olfr43 (Fig. 3c, d)		Validated odorant binding positions in other OR (or other odorants) ^d
	OR1A1	Olfr43	I (R)-(-)-carvone	II (S)-(+) -carvone	I (R)-(-)-carvone	II (S)-(+) -carvone	
TMH3	9 ^{b,c} Ala106 ^{3,34}	Gly	Indirect spatial 106 ↔ 152	Gly111: [73]			
	11 ^{b,c} Gly108 ^{3,36}	Ala	Direct steric	Direct steric	Direct steric	Direct steric hindrance	Ile112: [23], Val111: [74], Ile112: [75], Gly108: [16, 62], Val109: [25], Gly108: [22]
	12 ^{b,c} Asn109 ^{3,37}	Asn	H-bond	H-bond	H-bond	Not accessible	Val113: [23], Val113: [75], Asn109: [22]
	14 ^c Asp111 ^{3,39}	Asp	Indirect spatial 111 ↔ 250	–			
TMH4	12 ^{b,c} Gly152 ^{4,53}	Ala	Indirect spatial 152 ↔ 106	Ser156: [23]			
	15 ^c Asn155 ^{4,56}	Asn	Indirect spatial 155 ↔ 109	Ile159: [23], Ser155: [22]			
TMH5	9 ^{b,c} Ile205 ^{5,46[5,45]}	Val	Direct steric	Direct steric	Direct steric	Direct steric	Asn210: [23], Asn207: [24, 76], Asn207: [25], Phe206: [26], Ile205: [22] [Phe206: [25]], [Phe209: [60]], [Leu210: [60]]
TMH6	11 ^c Tyr250 ^{6,43}	Tyr	Indirect hydrophobic 250 ↔ 111 250 ↔ 276	Phe254: [74], Phe252: [24, 76], Phe252: [25]			
	12 ^{b,c} Tyr251 ^{6,44}	Tyr	Direct hydrophobic	Direct hydrophobic	Direct hydrophobic	Direct hydrophobic	Tyr252: [16, 62], Tyr256: [60], Tyr251: [22]
	TMH7	8 ^c Tyr276 ^{7,41}	Tyr	Direct hydrophobic 276 ↔ 250 276 ↔ 277			
TMH7	9 ^{b,c} Thr277 ^{7,42}	Thr	Indirect hydrophobic 277 ↔ 276	Thr277: [22], Thr279: [10], Thr279: [26]			

^a HORDE [51]^b Proposed amino acid positions constituting an odorant binding site [20]^c Carvone binding site in OR1A1 and Olfr43^d ORs' individual amino acid position numbering may deviate from the numbers of the alignment (compare Fig. S1)

depicts the amino acids constituting the carvone binding pocket in OR1A1 in a schematic snake diagram (Fig. 8a), and the conservation-deduced sequence logos of TMH1-7 and ECL2 (Fig. 8b).

Interestingly, for the 11 binding pocket-associated amino acid positions identified in this study, their conservation across all 37 mammalian species investigated was $83.2 \pm 28.7\%$, whereas in five hominids, their conservation was 96.4 ± 8.1 . Strikingly, and in contrast to a

previous study [20], the two binding pocket-associated positions Ile205^{5,46} and Thr277^{7,42}, which both had an impact on the carvone enantioselectivity in our study, revealed a conservation across 37 mammalian species of only 28.9 and 23.7%, respectively (Fig. 8b; Table 2). Notably, in OR1A1 orthologs, both Ile205^{5,46} and Thr277^{7,42} occur together exclusively in the five hominid sequences investigated (Fig S7), and are 100% conserved here (Table 2).

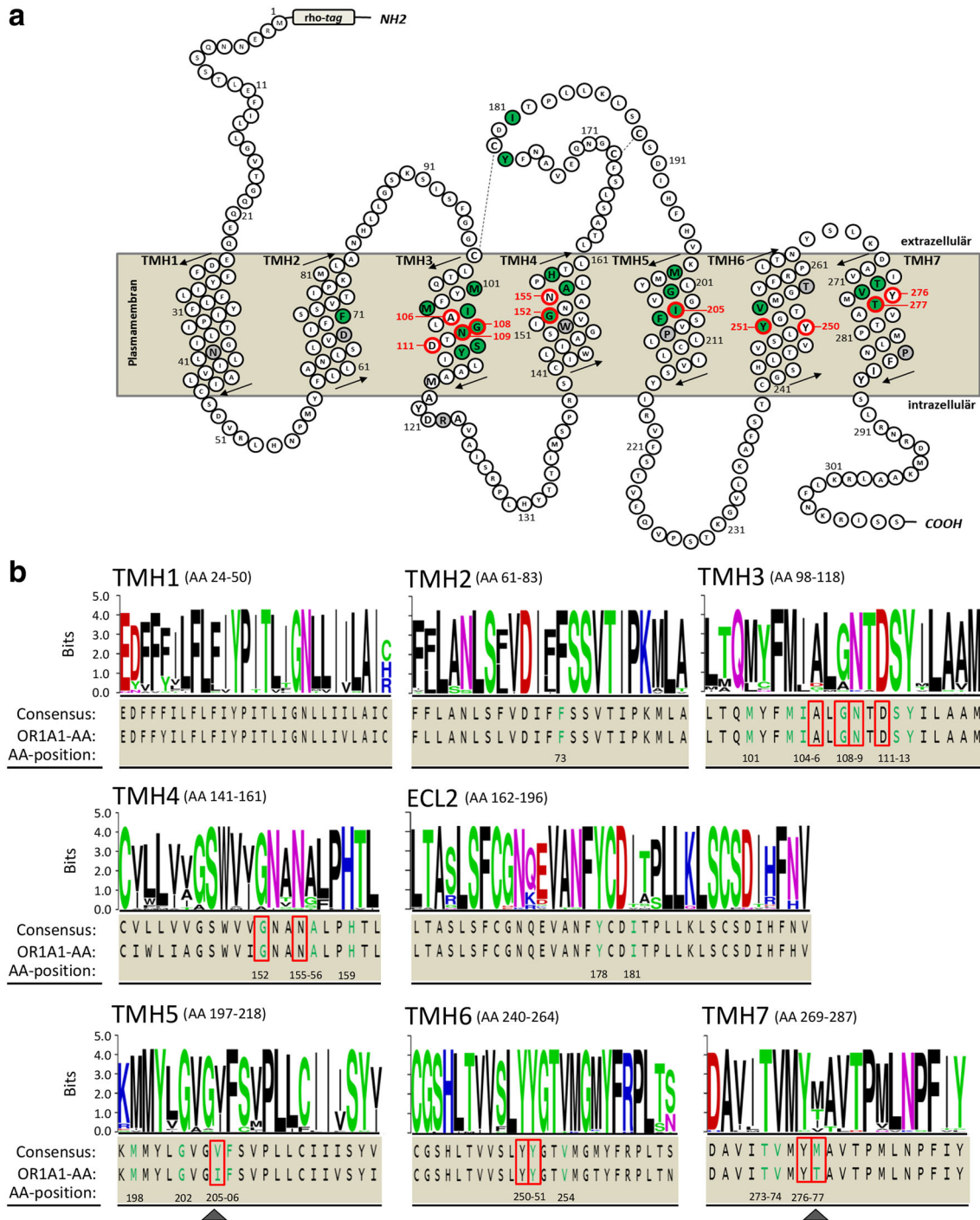


Fig. 8 Carvone-binding residues are conserved among OR1A1 orthologs. **a** Snake diagram of human OR1A1 with putative odorant binding site by [20] (green filled circles) and carvone binding site (red circles). Overlapping amino acid residues are shown as green filled red circles. Carvone binding site residues are Ala106^{3,34}, Gly108^{3,36}, Asn109^{3,37}, Asp111^{3,39}, Gly152^{4,53}, Asn155^{4,56}, Ile205^{5,46}, Tyr250^{6,43}, Tyr251^{6,44}, and Tyr276^{7,41}. The numbers refer to human OR1A1 amino acid sequence. **b** Alignments of transmembrane helices (TMH1-7) and extracellular loop 2 (ECL2) of human OR1A1, and its 37 orthologs. Shown are sequence logos, the consensus sequence, and the human OR1A1 sequence with the marked putative

odorant binding site by Ref. [20] (green letters) and carvone binding site (red boxes). Overlapping residues are shown as green letters in red boxes. The consensus amino acid refers to the most frequent one, which is determined by letter height and stacking order. The letters of each stack are ordered from the most frequent to the least frequent. Amino acid conservation is measured in bits, and a 100% conservation correlates to 4.32 bits [49]. Basic amino acids (K, R, H) are blue, polar (G, S, T, Y, C) are green, hydrophilic (Q, N) are purple, acidic (D, E) are red, and hydrophobic (A, V, L, I, P, W, M, F) are black. A complete phylogenetic tree of all reference sequences investigated, as well as their accession numbers are given in Fig S7 and Tab S1

Table 2 Amino acid conservation among OR1A1 orthologs

AA-position within TMH/ ECL segment ^a	Mutagenesis-validated carvone binding site positions within a proposed odorant binding pocket	AA-conservation [%] among OR1A1 orthologs (37 mammalian species)	AA-variations among OR1A1 orthologs	AA-conservation [%] among OR1A1 orthologs (5 hominids)	Correlated complementary interaction in model
TMH2 13	Phe73 ^b	100.0	—	100.0	
TMH3 4	Met101 ^b	84.2	M ₁₀₁ L	100.0	
7	Met104 ^b	100.0	—	100.0	
8	Ile105 ^b	92.1	I ₁₀₅ L	100.0	
9	Ala106^c	86.8	A ₁₀₆ G, A ₁₀₆ D, A ₁₀₆ T	80.0	106 ↔ 152
11	Gly108^{b,c}	84.2	G ₁₀₈ A, G ₁₀₈ S	100.0	—
12	Asn109^{b,c}	100.0	—	100.0	109 ↔ 155
14	Asp111^c	100.0	—	100.0	111 ↔ 250
15	Ser112 ^b	100.0	—	100.0	
16	Tyr113 ^b	100.0	—	100.0	
TMH4 12	Gly152^{b,c}	94.7	G ₁₅₂ A	100.0	152 ↔ 106
15	Asn155^c	100.0	—	100.0	155 ↔ 109
16	Ala156 ^b	78.9	A ₁₅₆ S, A ₁₅₆ G, A ₁₅₆ T	100.0	
19	His159 ^b	100.0	—	100.0	
ECL2 C-1	Tyr178 ^b	100.0	—	100.0	
C + 2	Ile181 ^b	92.1	I ₁₈₁ V, I ₁₈₁ T	100.0	
TMH5 2	Met198 ^b	94.7	M ₁₉₈ I, M ₁₉₈ V	100.0	
6	Gly202 ^b	100.0	—	100.0	
9	Ile205^{b,c}	28.9	I ₂₀₅ V	100.0	—
10	Phe206 ^b	100.0	—	100.0	
TMH6 11	Tyr250^c	100.0	—	100.0	250 ↔ 111/276
12	Tyr251^{b,c}	100.0	—	100.0	—
15	Val254 ^b	100.0	—	100.0	
TMH7 5	Thr273 ^b	100.0	—	100.0	
6	Val274 ^b	100.0	—	100.0	
8	Tyr276^c	97.4	Y ₂₇₆ C	80.0	276 ↔ 250/277
9	Thr277^{b,c}	23.7	T ₂₇₇ M, T ₂₇₇ I, T ₂₇₇ V	100.0	277 ↔ 276

^a HORDE [51]^b Proposed amino acid positions constituting an odorant binding site [20]^c Carvone binding site residues in OR1A1 and Olfr43, this study, printed in bold

Discussion

ORs discriminate between odorants of different physico-chemical properties, but also may distinguish different shapes, for example stereo enantiomers, of chemically highly similar odorants [39, 40, 59]. Recently, we characterized OR1A1 as an enantioselective receptor. In screening experiments with stereo enantiomers of carvone and menthone against all human ORs, OR1A1 was the only receptor that responded to both stereo enantiomers of both terpenoids [39, 40], suggesting OR1A1 to be crucially

involved in an enantioselective detection and discrimination of certain terpenoid odorants. OR1A1, however, is a broadly tuned receptor, capable of detecting a variety of chemically diverse KFO and non-KFO [7, 42]. The ability of an OR to distinguish between different odorants may result from distinct or partially overlapping binding sites [60, 61], within a mostly hydrophobic odorant binding pocket of the same receptor [22, 25].

Given the lack of high-resolution crystallographic information for ORs, the combination of site-directed mutagenesis, functional experimental analysis, in silico

homology modeling and docking simulation has been a valid tool to rationalize the molecular basis of odorant structure–activity and OR structure–function relationships [16, 22–26, 28, 62]. The choice of a GPCR experimental structure as template for computational homology modeling and docking simulation, however, has been a matter of debate [16], including a variety of different GPCR as single templates [63, 64], rhodopsin [18, 20, 22, 23, 25, 26, 60], opsin [65], and the β_2 -adrenergic receptor [24]. Thus, in this study, we applied a two-step modeling strategy. We not only used a fragment-based multi-template approach for each TMH [52, 53], but also we considered OR-specific proline patterns in TMH6 and TMH7 of human OR1A1 and murine Olfr43, which are responsible for distinct proline-caused kink-conformations that differ from currently available GPCR structures. Given the fact that, unlike as for class A GPCRs, no crystal structures of ORs or close homologues are available, these modified kink-conformations adapted to the OR1A1 and Olfr43 models may be afflicted with slight uncertainties concerning the TMH6 and TMH7 backbone. However, they enabled to explain our experimental findings and also provided a suitable basis for model-guided mutagenesis. Therefore, although TMH6 of ORs exhibits a different proline pattern, and thus a slightly altered conformation, it might be possible that Tyr²⁵¹^{6,44} of the “FYG” motif in ORs (Tyr^{6,48} as depicted in the work by DeMarch et al. [62]) corresponds to Phe^{6,44} in Class A GPCRs, which has been shown to be part of the activation relevant “PIF” (Pro^{5,50}; Ile^{3,40}; Phe^{6,44}) or “catalytic” motif [66].

The mutation of even single amino acids within a receptor may have severe effects on the tertiary structure, or the coupling to, for instance, G proteins or chaperones, and hence, in many cases, may result in a loss of receptor function, or may interfere with the proper trafficking of the receptor to the cell surface [67–69]. However, in the present study, we measured the cell surface expression of wild-type and mutant receptors, and showed that the modification of amino acids within the OR1A1, Olfr43, or btOR1A1 receptor did not interfere with their trafficking to the cell surface.

Moreover, the combination of site-directed mutagenesis, homology modeling, and *in silico* docking, which we used in our study, revealed not only a loss-of-function, but also a gain-of-function of the mutated receptors, as predicted and depending on mutual opposed changes of amino acids within the carvone binding pocket between OR1A1 and Olfr43, as well as between OR1A1 and btOR1A1.

Our functional expression experiments with OR1A1 homologs revealed that a carvone function was largely conserved across all OR1A1 orthologs tested, but not for its paralog OR1A2. This is comparable with the fact that ligand spectra between orthologous ORs are more

conserved than between paralogous ORs [43, 70]. In contrast to a previous study by Man et al. that proposed 22 amino acids to constitute a generalized odorant binding pocket [20], reconstituting these 22 amino acids from OR1A1 into the paralog OR1A2, in our hands, was not sufficient to establish any carvone function in OR1A2. This suggests that other amino acid positions are necessary for the enantioselective carvone responsiveness of OR1A1. Indeed, the 11 amino acids constituting a carvone binding pocket within OR1A1 identified in this study, overlap to just about 50% with those previously shown to be highly conserved among certain orthologs and predicted to constitute a generalized odorant binding pocket [20].

Sequence alignment of OR1A1 with its human paralog OR1A2, as well as with 36 mammalian orthologs, revealed high conservation for nine out of 11 identified carvone binding pocket residues. Two amino acids, Ile²⁰⁵^{5,46} and Thr²⁷⁷^{7,42}, surprisingly are not conserved at all across the 37 mammalian OR1A1 orthologous sequences investigated. In contrast, the combination of both Ile²⁰⁵^{5,46} and Thr²⁷⁷^{7,42} is exclusively apparent and 100% conserved in hominids. Indeed, just changing these two positions in bovine OR1A1 (btOR1A1) to the respective amino acid of the human receptor, rendered btOR1A1 a super-optimal, enantioselective carvone receptor.

Altogether, this suggests that generalized odorant binding pockets in ORs [20, 56] at best are models that need to be tested experimentally with respect to receptor activities and response to odorants. While these models consistently point to odorant binding within TMH2-TMH7, species-specific or other phylogenetic clade-specific amino acid conservancies at particular positions may override these generalized binding pocket predictions.

However, caution is advised regarding the sequence alignments, since the current NCBI reference sequences of ORs may still be provisional and may change after, for instance, validation of sequence, or frequency within populations [71].

Moreover, in this and a previous study [40], we have shown that both human and chimp OR1A1 are capable of detecting both enantiomers of several monocyclic terpenes, for instance carvone, limonene, and menthone. Here, we have shown that binding pocket-associated point mutations resulted in OR1A1 variants with severely altered phenotypes. In particular, position Thr²⁷⁷^{7,42} in the human OR1A1 is affected in a double-SNP haplotype (V₂₃₃M/T₂₇₇M) with a frequency of 2.7% [3, 57, 72]. Altogether, this suggests that OR1A1 is likely to be involved in the detection and discrimination of terpenoid enantiomers. The role of OR1A1 and its haplotypes in constituting a specific anosmia for (*R*)-(*–*)-carvone remains to be investigated in a further study. Indeed, the rather low frequency of the position 277-associated, SNP-

based OR1A1 haplotype suggests additional SNPs and/or other receptors that may be involved in a mechanism underlying the specific anosmia for (*R*)(*-*)-carvone in 8% of humans.

Our model newly identified the conserved residues Asn109^{3,37}, Tyr251^{6,44}, and Tyr276^{7,41} as key players in human OR1A1 for the detection of both carvone enantiomers. It also characterized the variant positions 108^{3,36}, 205^{5,46} as direct and 106^{3,34}, 152^{4,53}, as well as 277^{7,42} as indirect molecular determinants in OR1A1. In the present study, in line with other works (Table 1, for review, see Ref. [62]), position 108^{3,36} in ORs appeared to be generally important for a size-dependent, direct steric interaction with odorants. Therewith, we identified for the first time residues that contribute to the discrimination between carvone enantiomers, favoring (*R*)(*-*)- over (*S*)(*+*)-carvone.

Our model predicted direct steric interactions of position 205^{5,46} with both carvones in the human and murine receptors, as did a previous model by Man et al. [20]. However, a single mutation just on position 205^{5,46} to valine or isoleucine, in the human or murine receptor, respectively, had a little impact on the receptors' function. Vice versa, our carvone binding pocket model for OR1A1 is able to relate the deleterious effect of coding SNP position Thr277^{7,42}. Site-directed mutagenesis combined with functional expression of receptor variants demonstrated the loss-of-function phenotype of coding SNP T₂₇₇M on the carvone function of OR1A1. Altogether, this demonstrates the necessity of combining homology modeling, docking studies, site-directed mutagenesis, and functional expression of receptor variants for an understanding of enantioselective structure–function relations of ORs, given the lack of an OR crystal structure.

In summary, our data suggest 11 amino acid positions to directly and indirectly constitute an enantiomer-selective carvone binding pocket, necessary for a carvone function in human OR1A1 and its mouse ortholog Olfr43 (see Table 1; Supplemental Figure S1). Of those, 5 amino acid positions interact directly with the carvones, either by forming an H-bond (Asn109^{3,37}), in a sterical way (Gly108^{3,36}; Ile205^{5,46}), or by means of a hydrophobic interaction (Tyr251^{6,44}; Tyr267^{7,41}). We identified four of the five OR1A1 positions, that interact directly with the carvones, also in a previous study as interaction partners for citronellic terpenoids in OR1A1 and Olfr43 [22], and others have validated or suggested these for different OR/odorant combinations (see Table 1; Supplemental Figure S1). Of the 11 carvone-interacting positions, six interact indirectly, either by spatial or hydrophobic means, of which we identified only two as citronellic terpenoid binding pocket positions in OR1A1 in a previous study [22].

Moreover, we identified a carvone binding pocket-associated loss-of-function SNP haplotype of OR1A1, and elucidated possible OR-related mechanisms underlying an ability to discriminate between an enantiomer-related minty and caraway odor.

A full validation of our docking model for the carvone enantiomers, however, may require information on the crystal structure of OR1A1 in its active state. The combination of OR/GPCR homology modeling, site-directed mutagenesis, and functional expression studies so far provides a valid tool to elucidate the structure–function relations of OR.

Acknowledgements We thank Matthias Kotthoff for the initial experiments, and Julia Fiedler for expert technical assistance.

References

- Dunkel A, Steinhaus M, Kotthoff M, Nowak B, Krautwurst D, Schieberle P, Hofmann T (2014) Nature's chemical signatures in human olfaction: a foodborne perspective for future biotechnology. *Angew Chem Int Ed Engl* 53(28):7124–7143
- Krautwurst D, Kotthoff M (2013) A hit map-based statistical method to predict best ligands for orphan olfactory receptors: natural key odorants versus “lock picks”. *Methods Mol Biol* (Clifton, NJ) 1003:85–97
- Olender T, Lancet D, Nebert DW (2008) Update on the olfactory receptor (OR) gene superfamily. *Hum Genom* 3(1):87–97
- Buck L, Axel R (1991) A novel multigene family may encode odorant receptors: a molecular basis for odor recognition. *Cell* 65(1):175–187
- Kato A, Touhara K (2009) Mammalian olfactory receptors: pharmacology, G protein coupling and desensitization. *Cell Mol Life Sci* 66(23):3743–3753
- Verbeurg C, Wilkin F, Tarabichi M, Gregoire F, Dumont JE, Chatelain P (2014) Profiling of olfactory receptor gene expression in whole human olfactory mucosa. *PLoS One* 9(5):e96333
- Geithe C, Noe F, Kreissl J, Krautwurst D (2017) The broadly tuned odorant receptor OR1A1 is highly selective for 3-methyl-2,4-nonanedione, a key food odorant in aged wines, tea, and other foods. *Chem Senses* 42(3):181–193
- Malnic B, Hirono J, Sato T, Buck LB (1999) Combinatorial receptor codes for odors. *Cell* 96(5):713–723
- Nara K, Saraiva LR, Ye X, Buck LB (2011) A large-scale analysis of odor coding in the olfactory epithelium. *J Neurosci* 31(25):9179–9191
- Charlier L, Topin J, Ronin C, Kim SK, Goddard WA 3rd, Efremov R, Golebiowski J (2012) How broadly tuned olfactory receptors equally recognize their agonists. Human OR1G1 as a test case. *Cell Mol Life Sci* 69(24):4205–4213
- Laska M (2004) Olfactory discrimination ability of human subjects for enantiomers with an isopropenyl group at the chiral center. *Chem Senses* 29(2):143–152
- Laska M, Teubner P (1999) Olfactory discrimination ability for homologous series of aliphatic alcohols and aldehydes. *Chem Senses* 24(3):263–270
- Joshi D, Volkl M, Shepherd GM, Laska M (2006) Olfactory sensitivity for enantiomers and their racemic mixtures—a comparative study in CD-1 mice and spider monkeys. *Chem Senses* 31(7):655–664

14. Laska M, Liesen A, Teubner P (1999) Enantioselectivity of odor perception in squirrel monkeys and humans. *Am J Physiol* 277(4 Pt 2):R1098–R1103
15. Pelosi P, Viti R (1978) Specific anosmia to α -carvone—minty primary odor. *Chem Senses Flavour* 3(3):331–337
16. de March CA, Kim SK, Antonczak S, Goddard WA 3rd, Golebiowski J (2015) G protein-coupled odorant receptors: from sequence to structure. *Protein Sci* 24(9):1543–1548
17. Vaidehi N, Floriano WB, Trabanino R, Hall SE, Freddolino P, Choi EJ, Zamanakos G, Goddard WA 3rd (2002) Prediction of structure and function of G protein-coupled receptors. *Proc Natl Acad Sci USA* 99(20):12622–12627
18. Lai PC, Crasto CJ (2012) Beyond modeling: all-atom olfactory receptor model simulations. *Front Genet* 3:61
19. Charlier L, Topin J, de March CA, Lai PC, Crasto CJ, Golebiowski J (2013) Molecular modelling of odorant/olfactory receptor complexes. *Methods Mol Biol* (Clifton, NJ) 1003:53–65
20. Man O, Gilad Y, Lancet D (2004) Prediction of the odorant binding site of olfactory receptor proteins by human-mouse comparisons. *Protein Sci* 13(1):240–254
21. Liu AH, Zhang X, Stolovitzky GA, Califano A, Firestein SJ (2003) Motif-based construction of a functional map for mammalian olfactory receptors. *Genomics* 81(5):443–456
22. Schmiedeberg K, Shirokova E, Weber H-P, Schilling B, Meyerhof W, Krautwurst D (2007) Structural determinants of odorant recognition by the human olfactory receptors OR1A1 and OR1A2. *J Struct Biol* 159(3):400–412
23. Abaffy T, Malhotra A, Luetje CW (2007) The molecular basis for ligand specificity in a mouse olfactory receptor: a network of functionally important residues. *J Biol Chem* 282(2):1216–1224
24. Baud O, Etter S, Spreafico M, Bordoli L, Schwede T, Vogel H, Pick H (2011) The mouse eugenol odorant receptor: structural and functional plasticity of a broadly tuned odorant binding pocket. *Biochemistry* 50(5):843–853
25. Katada S, Hirokawa T, Oka Y, Suwa M, Touhara K (2005) Structural basis for a broad but selective ligand spectrum of a mouse olfactory receptor: mapping the odorant-binding site. *J Neurosci* 25(7):1806–1815
26. Gelis L, Wolf S, Hatt H, Neuhaus EM, Gerwert K (2012) Prediction of a ligand-binding niche within a human olfactory receptor by combining site-directed mutagenesis with dynamic homology modeling. *Angew Chem Int Ed Engl* 51(5):1274–1278
27. Sekharan S, Ertem Mehmed Z, Zhuang H, Block E, Matsunami H, Zhang R, Wei Jennifer N, Pan Y, Batista Victor S (2014) QM/MM model of the mouse olfactory receptor MOR244-3 validated by site-directed mutagenesis experiments. *Biophys J* 107(5):L5–L8
28. Li S, Ahmed L, Zhang R, et al (2016) Smelling sulfur: copper and silver regulate the response of human odorant receptor OR2T11 to low-molecular-weight thiols. *J Am Chem Soc* 138(40):13281–13288. doi:[10.1021/jacs.6b06983](https://doi.org/10.1021/jacs.6b06983)
29. Bakalyar HA, Reed RR (1990) Identification of a specialized adenylyl cyclase that may mediate odorant detection. *Science* 250(4986):1403–1406
30. Levy NS, Bakalyar HA, Reed RR (1991) Signal transduction in olfactory neurons. *J Steroid Biochem Mol Biol* 39(4B):633–637
31. Wong ST, Trinh K, Hacker B, Chan GC, Lowe G, Gaggar A, Xia Z, Gold GH, Storm DR (2000) Disruption of the type III adenylyl cyclase gene leads to peripheral and behavioral anosmia in transgenic mice. *Neuron* 27(3):487–497
32. Zou DJ, Chesler AT, Le Pichon CE, Kuznetsov A, Pei X, Hwang EL, Firestein S (2007) Absence of adenylyl cyclase 3 perturbs peripheral olfactory projections in mice. *J Neurosci* 27(25):6675–6683
33. Pace U, Hanski E, Salomon Y, Lancet D (1985) Odorant-sensitive adenylyl cyclase may mediate olfactory reception. *Nature* 316(6025):255–258
34. Krautwurst D (2008) Human olfactory receptor families and their odorants. *Chem Biodivers* 5(6):842–852
35. Krautwurst D, Yau KW, Reed RR (1998) Identification of ligands for olfactory receptors by functional expression of a receptor library. *Cell* 95(7):917–926
36. Touhara K (2007) Deorphanizing vertebrate olfactory receptors: recent advances in odorant-response assays. *Neurochem Int* 51(2–4):132–139
37. Zhuang H, Matsunami H (2007) Synergism of accessory factors in functional expression of mammalian odorant receptors. *J Biol Chem* 282(20):15284–15293
38. Zhuang H, Matsunami H (2008) Evaluating cell-surface expression and measuring activation of mammalian odorant receptors in heterologous cells. *Nat Protoc* 3(9):1402–1413
39. Geithe C, Krautwurst D (2015) Chirality matters and SNPs make the difference—genetic variations on enantiomer-specific odorant receptors for carvone. In: Taylor AJ, Mottram DS (eds) Flavour science: proceedings of the XIV Weurman flavour research symposium, vol 14. 14. Context Products Ltd., Leicestershire, pp 297–302
40. Geithe C, Krautwurst D (2015) Chirality matters—enantioselective orthologous odorant receptors for related terpenoid structures. In: Engel K-H, Takeoka G (eds) Importance of chirality to flavor compounds, vol 1212. ACS Symposium Series, vol 1212. American Chemical Society, Washington, DC, pp 161–181
41. Binkowski B, Fan F, Wood K (2009) Engineered luciferases for molecular sensing in living cells. *Curr Opin Biotechnol* 20(1):14–18
42. Saito H, Chi Q, Zhuang H, Matsunami H, Mainland JD (2009) Odor coding by a Mammalian receptor repertoire. *Sci Signal* 2(60):ra9
43. Adipietro KA, Mainland JD, Matsunami H (2012) Functional evolution of mammalian odorant receptors. *PLoS Genet* 8(7):e1002821
44. Mainland JD, Keller A, Li YR, Zhou T, Trimmer C, Snyder LL, Moberly AH, Adipietro KA, Liu WL, Zhuang H, Zhan S, Lee SS, Lin A, Matsunami H (2014) The missense of smell: functional variability in the human odorant receptor repertoire. *Nat Neurosci* 17(1):114–120
45. Saito H, Kubota M, Roberts RW, Chi Q, Matsunami H (2004) RTP family members induce functional expression of mammalian odorant receptors. *Cell* 119(5):679–691
46. Shirokova E, Schmiedeberg K, Bedner P, Niessen H, Willecke K, Raguse JD, Meyerhof W, Krautwurst D (2005) Identification of specific ligands for orphan olfactory receptors. G protein-dependent agonism and antagonism of odorants. *J Biol Chem* 280(12):11807–11815
47. Jones DT, Reed RR (1989) Golf: an olfactory neuron specific-G protein involved in odorant signal transduction. *Science* 244(4906):790–795
48. Li F, Ponissery-Saidu S, Yee KK, Wang H, Chen ML, Iguchi N, Zhang G, Jiang P, Reisert J, Huang L (2013) Heterotrimeric G protein subunit Ggamma13 is critical to olfaction. *J Neurosci* 33(18):7975–7984
49. Crooks GE, Hon G, Chandonia JM, Brenner SE (2004) WebLogo: a sequence logo generator. *Genome Res* 14(6):1188–1190
50. Schneider TD, Stephens RM (1990) Sequence logos: a new way to display consensus sequences. *Nucleic Acids Res* 18(20):6097–6100
51. Safran M, Chalifa-Caspi V, Shmueli O, Olender T, Lapidot M, Rosen N, Shmoish M, Peter Y, Glusman G, Feldmesser E, Adato A, Peter I, Khen M, Atarot T, Groner Y, Lancet D (2003) Human gene-centric databases at the Weizmann Institute of Science: GeneCards, UDB, CroW 21 and HORDE. *Nucleic Acids Res* 31(1):142–146

52. Worth CL, Kleinau G, Krause G (2009) Comparative sequence and structural analyses of G-protein-coupled receptor crystal structures and implications for molecular models. *PLoS One* 4(9):e7011
53. Worth CL, Kreuchwig A, Kleinau G, Krause G (2011) GPCR-SSFE: a comprehensive database of G-protein-coupled receptor template predictions and homology models. *BMC Bioinform* 12:185
54. Worth CL, Kreuchwig F, Tiemann JKS, et al (2017) GPCR-SSFE 2.0-a fragment-based molecular modeling web tool for class A G-protein coupled receptors. *Nucleic Acids Res.* doi:[10.1093/nar/gkx399](https://doi.org/10.1093/nar/gkx399)
55. Ballesteros JA, Weinstein H (1995) Integrated methods for the construction of three-dimensional models and computational probing of structure–function relations in G protein-coupled receptors. In: Stuart CS (ed) *Methods in neurosciences*, vol 25. Academic Press, New York, pp 366–428
56. Pilpel Y, Lancet D (1999) The variable and conserved interfaces of modeled olfactory receptor proteins. *Protein Sci* 8(5):969–977
57. Genomes Project Consortium, Abecasis GR, Auton A, Brooks LD, DePristo MA, Durbin RM, Handsaker RE, Kang HM, Marth GT, McVean GA (2012) An integrated map of genetic variation from 1,092 human genomes. *Nature* 491(7422):56–65
58. Venkatakrishnan AJ, Deupi X, Lebon G, Tate CG, Schertler GF, Babu MM (2013) Molecular signatures of G-protein-coupled receptors. *Nature* 494(7436):185–194
59. Takai Y, Touhara K (2015) Enantioselective recognition of menthol by mouse odorant receptors. *Biosci Biotechnol Biochem* 79(12):1980–1986
60. Lai PC, Guida B, Shi J, Crasto CJ (2014) Preferential binding of an odor within olfactory receptors: a precursor to receptor activation. *Chem Senses* 39(2):107–123
61. Lai PC, Singer MS, Crasto CJ (2005) Structural activation pathways from dynamic olfactory receptor-odorant interactions. *Chem Senses* 30(9):781–792
62. de March CA, Yu Y, Ni MJ, Adipietro KA, Matsunami H, Ma M, Golebiowski J (2015) Conserved residues control activation of mammalian G protein-coupled odorant receptors. *J Am Chem Soc* 137(26):8611–8616
63. Cvicek V, Goddard WA 3rd, Abrol R (2016) Structure-based sequence alignment of the transmembrane domains of all human GPCRs: phylogenetic, structural and functional implications. *PLoS Comput Biol* 12(3):e1004805
64. Launay G, Teletchea S, Wade F, Pajot-Augy E, Gibrat JF, Sanz G (2012) Automatic modeling of mammalian olfactory receptors and docking of odorants. *Protein Eng Des Select* 25(8):377–386
65. Park JH, Morizumi T, Li Y, Hong JE, Pai EF, Hofmann KP, Choe HW, Ernst OP (2013) Opsin, a structural model for olfactory receptors? *Angew Chem Int Ed Engl* 52(42):11021–11024
66. Kobilka BK (2011) Structural insights into adrenergic receptor function and pharmacology. *Trends Pharmacol Sci* 32(4):213–218
67. McIntyre JC, Hege MM, Berbari NF (2016) Trafficking of ciliary G protein-coupled receptors. *Methods Cell Biol* 132:35–54
68. Nemet I, Ropelewski P, Imanishi Y (2015) Rhodopsin Trafficking and mistrafficking: signals, molecular components, and mechanisms. *Prog Mol Biol Transl Sci* 132:39–71
69. Young B, Wertman J, Dupre DJ (2015) Regulation of GPCR anterograde trafficking by molecular chaperones and motifs. *Prog Mol Biol Transl Sci* 132:289–305
70. Jiang Y, Matsunami H (2015) Mammalian odorant receptors: functional evolution and variation. *Curr Opin Neurobiol* 34C:54–60
71. Trimmer C, Mainland JD (2017) Simplifying the odor landscape. *Chem Senses* 42(3):177–179
72. HORDE. The Human Olfactory Receptor Data Exploratorium (HORDE) (2011) The Weizmann Institute. <http://bioportal.weizmann.ac.il/HORDE/>. Accessed 16 March 2015
73. Kurland MD, Newcomer MB, Peterlin Z, Ryan K, Firestein S, Batista VS (2010) Discrimination of saturated aldehydes by the rat 17 olfactory receptor. *Biochemistry* 49(30):6302–6304
74. Anselmi C, Buonocore A, Centini M, Facino RM, Hatt H (2011) The human olfactory receptor 17–40: requisites for fitting into the binding pocket. *Comput Biol Chem* 35(3):159–168
75. Bavan S, Sherman B, Luetje CW, Abaffy T (2014) Discovery of novel ligands for mouse olfactory receptor MOR42-3 using an in silico screening approach and in vitro validation. *PLoS One* 9(3):e92064
76. Baud O, Yuan S, Veya L, Filipek S, Vogel H, Pick H (2015) Exchanging ligand-binding specificity between a pair of mouse olfactory receptor paralogs reveals odorant recognition principles. *Sci Rep* 5:14948

Cellular & Molecular Life Sciences is a copyright of Springer, 2017. All Rights Reserved.